

Protonic thermoelectric effect of Superionic H₂O and magnetic field generation in Uranus and Neptune

Daohong Liu^{1,2}, Wei Zhang³, Yu He^{1,4,5*}, Xinzhan Guo^{1,4}, Chuanyu Zhang⁶, Yang Sun⁷

¹State Key Laboratory of Critical Mineral Research and Exploration, Institute of Geochemistry, Chinese Academy of Sciences, Guiyang 550081, China.

²College of Earth and Planetary Sciences, University of Chinese Academy of Sciences, Beijing 100049, China.

³School of Geography and Environmental Science (School of Karst Science), Guizhou Normal University, Guiyang 550025, China.

⁴Key Laboratory of High-Temperature and High-Pressure Study of the Earth's Interior, Institute of Geochemistry, Chinese Academy of Sciences, Guiyang 550081, Guizhou, China

⁵Center for High Pressure Science and Technology Advanced Research, Shanghai 201203, China.

⁶College of Physics, Chengdu University of Technology, Chengdu, 610059, China.

⁷School of Materials, Sun Yat-sen University, Shenzhen, China.

*Corresponding author. Email: heyu@mail.gyig.ac.cn

Abstract:

Uranus and Neptune are characterized by anomalously tilted and multi-dipole magnetic fields, which poses substantial challenges for elucidating the internal mechanisms generating magnetic fields. Recent investigations confirmed that superionic H₂O is thermodynamically stable and constitutes the dominant H₂O phase within their icy mantles. In this study, we demonstrate that the superionic H₂O ice exhibits a pronounced protonic thermoelectric effect, in which the maximum Seebeck coefficient within the interior of Uranus can reach approximately 620 $\mu\text{V}\cdot\text{K}^{-1}$, whereas that of Neptune is lower, within the range of 570–585 $\mu\text{V}\cdot\text{K}^{-1}$. Consequently, temperature gradients in the icy mantles can induce proton convection, which in turn drives magnetic field generation. Based on this novel mechanism, the disparities in magnetic field strength between Uranus and Neptune can be accounted for exclusively by their differing internal temperature gradients, and the predicted values are in agreement with observations.

Unlike the predominantly dipolar and nearly axisymmetric magnetic fields of terrestrial planets and gas giants (1), the magnetic fields of Uranus and Neptune exhibit significant non-dipole and non-axisymmetric characteristics, with their magnetic axes substantially offset from the planetary center and highly inclined relative to the rotation axis (2–7). This unique magnetic field configuration not only challenges conventional dynamo theory but also offers critical insights into the internal dynamics, material states, and evolutionary history of the ice giants. To explain the anomalous geometry of magnetic fields of Uranus and Neptune, Stanley and Bloxham (8) proposed the thin-shell dynamo model. It posits that the magnetic field is generated within a relatively thin, convecting fluid layer in the outer part of the icy mantles, beneath which lies a large, stably stratified region. This thin-shell geometry produces smaller-scale convection, thereby generating a multipolar magnetic field. For the thin-shell dynamo model, whether a stable stratification can form beneath the convective layer, as well as the mechanical and electrical properties of the underlying stratification, are also key factors for the stable generation of magnetic fields (5, 9). Alternatively, the magnetic field may be generated by internal turbulence that is not strongly constrained by the planet's rotation, thus leading to a multipolar field (10). Nevertheless, the lack of knowledge of the internal composition and transport properties of ice giants continues to impede our ability to discriminate among the magnetic field generation mechanisms and to identify the physical origin of the observed magnetic fields.

Interior structure models and high-pressure studies indicate that H_2O , CH_4 , and NH_3 ices are the dominant components in the interior of Uranus and Neptune (11–14). Recent high-pressure and high-temperature experiments have confirmed the superionic (SI) transition of H_2O and NH_3 under the interior conditions of Uranus and Neptune (12, 15–24). In SI ices, protons diffuse like a liquid through solid-like sublattices of heavier nuclei. This unique phase simultaneously exhibits shear stiffness and extremely high ionic conductivity (25, 26). In particular, SI H_2O ice undergoes a structural transition from a body-centered-cubic (bcc) to a face-centered-cubic (fcc) phase with increasing temperature, accompanied by a significant increase in ionic conductivity (17, 25). The entropy contributed by the highly diffusive protons leads to high stability of the SI fcc phase, which remains stable across most of the pressure-temperature (P - T) range of the icy mantles (21, 23, 27). These findings imply that the SI fcc H_2O ice is likely to be a major component of the icy mantles beneath the fluid H_2O layer. Therefore, its electrical and mechanical properties are proposed to influence the magnetic field generation in the ice giants (5, 26, 28–30).

Ionic thermoelectric (*i*-TE) refers to a thermoelectric effect based on ionic transport (31–35), specifically a physical phenomenon wherein charged ions in ionic conductors (such as solid electrolytes, gels, ionic liquids, etc.) undergo directed migration driven by a definite temperature gradient, thereby establishing a thermovoltage across the material (31, 33–35). The *i*-TE materials, which present high Seebeck coefficients rivaling tens of $\text{mV}\cdot\text{K}^{-1}$ (32, 33,), have been used for electric generation devices (36). Since SI H_2O ice is an effective proton conductor in the ice giants, the protonic thermoelectric (*p*-TE) mechanism could generate planetary-scale thermocurrents wherever a persistent thermal gradient exists. Such currents would not merely be a passive byproduct of interior dynamics but also influence the energy source and topology of magnetic fields.

In this study, we calculated ionic conductivity, thermal transport properties, and *p*-TE coefficients of SI H₂O under the conditions of the ice giants' interior using combined *ab initio* molecular dynamics (AIMD) and deep potential molecular dynamics (DPMD) methods. In addition, we also evaluated the potential impact of *p*-TE on planetary-scale magnetic field generation in Uranus and Neptune.

Density Profiles of Superionic H₂O Ice

We first evaluated our trained potential and computational method by comparing the pressure-temperature-density (*P-T-ρ*) relations of bcc and fcc H₂O calculated using AIMD and DPMD simulations at 150–450 GPa and 1000–4000 K (Figs. 1A, S1 and S2). The density profiles of bcc and fcc H₂O calculated using DPMD show great agreement with AIMD results. The accuracy of the DP model was further evaluated by comparing its predictions to AIMD results (Figs. S3–S5). The calculated densities are also consistent with experimental results using static (24) and dynamic (22) compression methods. In addition, we found that fcc H₂O becomes denser than bcc H₂O at pressures above ~200 GPa (Fig. 1A), indicating that bcc H₂O becomes less compressible with increasing temperature. This behavior leads to the fcc phase exhibiting relatively high stability in comparison with the bcc phase at high pressure, consistent with previous computational results (21).

Recent experimental studies have also emphasized the importance of volume expansion for the SI transition of both bcc and fcc H₂O (37). In this case, we determined the volume changes for bcc and fcc H₂O upon the SI transition at 200 GPa with refined temperature intervals (Fig. 1B). Indeed, the onset of SI state is accompanied with volume expansion. The SI transition in bcc ice occurs at 2250–2600 K, which is ~500 K higher than the transition in fcc phase, consistent with experimental observation (37). The thermal expansion coefficients α (Fig. 1C), obtained from the fitted curves, exhibits a characteristic λ -shaped peak associated with the onset of the SI transition. The calculated peak value of α in this study is within the range of previous predictions (21, 37). Our results confirm that the volume change upon the SI transition is critical for the determination of the SI transition temperature for experimental observations.

Protonic Thermoelectric in Superionic H₂O Ice

We calculated the thermal conductivities of bcc and fcc H₂O using the non-equilibrium molecular dynamics (NEMD) method (Figs. S6–S8). In bcc H₂O, the thermal conductivity exhibits an obvious decrease with increasing temperature (Fig. 2). This behavior can be attributed to intensified proton-phonon interactions driven by the SI transition (39), which substantially shorten the phonon mean free path (MFP), thereby suppressing thermal transport. In contrast, the fcc H₂O exhibits a near temperature-independent lattice thermal conductivity. This apparent insensitivity to temperature stems from a distinct transport mechanism in which the thermal conductivity is governed by lattice phonons whose MFPs are primarily limited by proton-phonon scattering. Due to the exceptionally high diffusivity of protons in the SI fcc phase (Fig. S9A), this scattering mechanism is intrinsically strong and nearly temperature-independent, resulting in a saturation of the phonon MFP and a suppression of temperature-dependent effects. Additionally, pressure has a monotonic enhancing effect on the thermal conductivity for both bcc and fcc H₂O. As pressure increases, atomic vibrations are increasingly constrained, reducing phonon scattering intensity and

promoting more efficient heat transport. Based on the thermal profiles of Uranus and Neptune, H₂O mainly exists in the form of SI fcc H₂O in icy mantles (Fig. S9). The highly diffusive protons in fcc H₂O lead to heat flux dispersion, thus decreasing the thermal conductivity efficiency in the interior of the ice giants.

We then calculated the temperature-dependent evolution of the proton diffusion coefficient by fitting the mean square displacements (MSDs) of protons under the internal *P-T* conditions relevant to Uranus and Neptune (Figs. S10–S12). The Nernst-Einstein equation is used to estimate the ionic conductivity of SI fcc H₂O ice, and the ionic conductivity scatter plots are fitted using the Arrhenius equation, as presented in Fig. 3A. It is worth noting that the ionic conductivity of SI fcc H₂O increases with rising pressure, which can be attributed to the increase in proton concentration. Although the proton diffusion coefficient decreases with pressure (Fig. S12), the magnitude of the increase in proton concentration exceeds the reduction in proton diffusivity, leading to an overall enhancement of ionic conductivity.

Furthermore, to elucidate the thermoelectric response of SI fcc H₂O, the Widom insertion method has been employed to compute the proton chemical potential, enabling us to determine the partial molar entropy of protons (Fig. 3B). Based on these values, we calculated the Seebeck coefficient of the SI fcc H₂O within the framework of Onsager relations (32) under the interior conditions of Uranus and Neptune (Fig. 3C). The SI fcc H₂O maintains a significant and relatively pressure-insensitive Seebeck response throughout the range of planetary interior conditions, underscoring the persistence of significant thermoelectric effect even in the deep interior of icy mantles. In the interior of ice giants, the Seebeck coefficient of fcc H₂O slightly increases with depth. The maximum Seebeck coefficient in Uranus can reach 620 $\mu\text{V}\cdot\text{K}^{-1}$, while in Neptune, the coefficient is lower, ranging between 570–585 $\mu\text{V}\cdot\text{K}^{-1}$. Importantly, the high Seebeck coefficient is complemented by exceptional ionic conductivity, resulting in a large thermoelectric power factor (Fig. 3D). Quantitative comparison reveals that the power factor of SI fcc H₂O surpasses that of many conventional ionic/electronic thermoelectric materials (Fig. S13) (34, 41, 42), suggesting that SI fcc H₂O may constitute an efficient mechanism for energy conversion and charge redistribution in planetary interiors. These findings highlight the important role of SI fcc H₂O in both magnetic field generation and heat dissipation in ice giants.

Geomagnetic fields generation in Uranus and Neptune

The highly eccentric and strongly non-dipolar magnetic field morphologies of Uranus and Neptune are thought to arise from a thin, active convective shell in their shallow interiors, overlain by a stable inner layer (8). A key implicit premise of this model is that the thin shell must simultaneously possess sufficiently high electrical conductivity and intense turbulent convection to sustain an effective global dynamo process. Shock compression and computational results suggest the conductivities of fluid H₂O in the interiors of icy giants exceed $\sim 1000 \text{ S/m}$ (17, 29, 43). However, recent static conductivity measurements of dense fluid H₂O indicate that the fluid H₂O in the shallow thin layer, with a low conductivity of 10–40 S/m, cannot meet the requirement of a magnetic Reynolds number $R_m > 40$. Therefore, for the traditional dynamo to operate, it is necessary to assume that the internal temperature is several thousand Kelvin higher than that predicted by adiabatic models (approximately 4300 K), enabling H₂O to enter an electronically conducting state

(44). Nevertheless, according to the internal thermodynamic models of Uranus and Neptune (40, 45), such high temperatures are nearly unattainable in the shallow ionic fluid layer. Thus, clarifying the electrical conductivity of fluid H₂O is critical to the mechanism of magnetic generation inside ice giants. Furthermore, recent observations and evolution models of ice giants have indicated that there are significant differences between the deep thermodynamic state and the full convection assumption of the dynamo model. Constraints from the interior structure and thermal evolution suggest that Uranus and Neptune may contain significant compositional gradients and thermal boundary layer structures (46–48), which might inhibit large-scale convection and result in a fainter radiated luminosity of Uranus (49). On the other hand, numerical simulations also show that complex chemical mixtures may form stable stratified regions under high pressure, resulting in heat transport efficiency lower than the model assumptions (7, 50).

Thermoelectricity describes the direct conversion of heat into electricity without mechanical motion. This mechanism may become particularly significant for planets where low heat flux is insufficient to drive the convection of conductive fluids. Furthermore, it has also been applied to understanding the generation of the geomagnetic field. (51). Here, we found that SI fcc H₂O, which occupies the icy mantles region above the rocky cores of Uranus and Neptune (Figs. 4A and 4B), presents significant the *p*-TE effect. Therefore, proton convection can be driven by the temperature gradient inside the ice giants. Based on proton convection induced by the steady-state temperature gradient across the adiabatic boundary layer, we utilized the Biot-Savart-Laplace law to calculate the planetary surface magnetic field strength under the *p*-TE conversion efficiency of 2.5%. By combining calculations of electrical conductivity along the internal thermal profiles of Uranus and Neptune, we fitted and annotated the contours of their internal ionic conductivity (σ) and temperature gradient ($\nabla_r T$) relationship in the diagram (Figs. S14–S17), as shown in Fig. 4C. The results indicate that within the estimated range for Uranus's interior, the corresponding magnetic field strength values primarily fall near the 20–25 μ T contour lines, which are in good agreement with the Uranus averaged surface magnetic field strength (23 μ T) inverted by Voyager (2). On the other hand, the calculated magnetic field strength based on the σ - $\nabla_r T$ relation for Neptune is distributed between 15–20 μ T and is also consistent with the observed average magnetic field strength of Neptune (13 μ T) (3). It is noteworthy that differences in the thermodynamic conditions of Uranus and Neptune produce distinct internal temperature gradients and electrical conductivity distributions, which in turn lead to the different magnetic field strengths, reflecting that Uranus can obtain a slightly higher average surface field strength than Neptune. This trend not only aligns with observations but also demonstrates that the thermoelectric circuit can naturally distinguish the magnetic field strengths of Uranus and Neptune.

The *p*-TE mechanism provides a new perspective on the origin of the magnetic fields in ice giants. This mechanism can be driven solely by internal temperature gradients, which does not require vigorous convective motions. Although *p*-TE can generate significant magnetic field strengths comparable to the observations, our calculation only considers the thermoelectric currents generated by a single component of fcc SI H₂O. In reality, the true composition of the icy mantles might be mixed with complex ices such as NH₃ and CH₄. Recent studies also suggest possible reactions between H₂O and rocks to generate SI hydrous phases (14, 52, 53). This complex compositional heterogeneity leads to variations in local electrical and thermal conductivity, which in turn may cause variations of Seebeck coefficients in the icy mantles. In addition, lateral variations in temperature of the icy mantles may also lead to spatial fluctuations in the temperature

gradient. The inhomogeneity caused by compositional differences and variations in temperature gradients in the icy mantles may affect the strength and direction of the *p*-TE current, resulting in spatially complex magnetic fields of Uranus and Neptune.

References and Notes

1. C. T. Russell, Magnetic fields of the terrestrial planets. *J. Geophys. Res. Planets* 98, 18681–18695 (1993).
2. N. F. Ness, M. H. Acuña, K. W. Behannon, L. F. Burlaga, J. E. P. Connerney, R. P. Lepping, F. M. Neubauer, Magnetic Fields at Uranus. *Science* 233, 85–89 (1986).
3. N. F. Ness, M. H. Acuña, L. F. Burlaga, J. E. P. Connerney, R. P. Lepping, F. M. Neubauer, Magnetic Fields at Neptune. *Science* 246, 1473–1478 (1989).
4. G. Schubert, K. M. Soderlund, Planetary magnetic fields: Observations and models. *Phys. Earth Planet. Inter.* 187, 92–108 (2011).
5. R. Redmer, T. R. Mattsson, N. Nettelmann, M. French, The phase diagram of water and the magnetic fields of Uranus and Neptune. *Icarus* 211, 798–803 (2011).
6. C. Paty, C. S. Arridge, I. J. Cohen, G. A. DiBraccio, R. W. Ebert, A. M. Rymer, Ice giant magnetospheres. *Phil. Trans. R. Soc. A* 378, 20190480 (2020).
7. K. M. Soderlund, S. Stanley, The underexplored frontier of ice giant dynamos. *Phil. Trans. R. Soc. A* 378, 20190479 (2020).
8. S. Stanley, J. Bloxham, Convective-region geometry as the cause of Uranus' and Neptune's unusual magnetic fields. *Nature* 428, 151–153 (2004).
9. B. Militzer, Phase separation of planetary ices explains nondipolar magnetic fields of Uranus and Neptune. *Proc. Natl. Acad. Sci.* 121, e2403981121 (2024).
10. K. Soderlund, M. Heimpel, E. King, J. Aurnou, Turbulent models of ice giant internal dynamics: Dynamos, heat transfer, and zonal flows. *Icarus* 224, 97–113 (2013).
11. M. Podolak, A. Weizman, M. Marley, Comparative models of Uranus and Neptune. *Planet. Space Sci.* 43, 1517–1522 (1995).
12. J.-A. Hernandez, M. Bethkenhagen, S. Ninet, M. French, A. Benuzzi-Mounaix, F. Datchi, M. Guaraguaglini, F. Lefevre, F. Occelli, R. Redmer, T. Vinci, A. Ravasio, Melting curve of superionic ammonia at planetary interior conditions. *Nat. Phys.* 19, 1280–1285 (2023).
13. A. F. Goncharov, N. Goldman, L. E. Fried, J. C. Crowhurst, I. -F. W. Kuo, C. J. Mundy, and J. M. Zaug, Dynamic ionization of water under extreme conditions. *Phys. Rev. Lett.* 94, 125508 (2005).
14. K. de Villa, F. González-Cataldo, B. Militzer, Double superionicity in icy compounds at planetary interior conditions. *Nat. Commun.* 14, 7580 (2023).
15. C. Cavazzoni, G. L. Chiarotti, S. Scandolo, E. Tosatti, M. Bernasconi, M. Parrinello, Superionic and metallic states of water and ammonia at giant planet conditions. *Science* 283, 44–46 (1999).
16. E. Katoh, H. Yamawaki, H. Fujihisa, M. Sakashita, K. Aoki, Protonic diffusion in high-pressure ice VII. *Science* 295, 1264–1266 (2002).

17. M. French, S. Hamel, R. Redmer, Dynamical screening and ionic conductivity in water from ab initio simulations. *Phys. Rev. Lett.* 107, 185901 (2011).
18. J. -A. Hernandez, R. Caracas, Superionic-superionic phase transitions in body-centered cubic H₂O ice. *Phys. Rev. Lett.* 117, 135503 (2016).
19. M. Millot, S. Hamel, J. R. Rygg, P. M. Celliers, G. W. Collins, F. Coppapi, D. E. Fratanduono, R. Jeanloz, D. C. Swift, J. H. Eggert, Experimental evidence for superionic water ice using shock compression. *Nat. Phys.* 14, 297–302 (2018).
20. J.-A. Queyroux, J. -A. Hernandez, G. Weck, S. Ninet, T. Plisson, S. Klotz, G. Garbarino, N. Guignot, M. Mezouar, M. Hanfland, J.-P. Itié, F. Datchi, Melting curve and isostructural solid transition in superionic ice. *Phys. Rev. Lett.* 125, 195501 (2020).
21. B. Cheng, M. Bethkenhagen, C. J. Pickard, S. Hamel, Phase behaviours of superionic water at planetary conditions. *Nat. Phys.* 17, 1228–1232 (2021).
22. M. Millot, F. Coppapi, J. R. Rygg, A. Correa Barrios, S. Hamel, D. C. Swift, J. H. Eggert, Nanosecond X-ray diffraction of shock-compressed superionic water ice. *Nature* 569, 251–255 (2019).
23. V. B. Prakapenka, N. Holtgrewe, S. S. Lobanov, A. F. Goncharov, Structure and properties of two superionic ice phases. *Nat. Phys.* 17, 1233–1238 (2021).
24. G. Weck, J. -A. Queyroux, S. Ninet, F. Datchi, M. Mezouar, P. Loubeyre, Evidence and stability field of fcc superionic water ice using static compression. *Phys. Rev. Lett.* 128, 165701 (2022).
25. S. Sun, Y. He, D. Y. Kim, H. Li, Anomalous elastic properties of superionic ice. *Phys. Rev. B* 102, 104108 (2020).
26. F. Matusalem, J. Santos Rego, M. de Koning, Plastic deformation of superionic water ices. *Proc. Natl. Acad. Sci.* 119, e2203397119 (2022).
27. R. J. Husband, H. P. Liermann, J. D. McHardy, R. S. McWilliams, A. F. Goncharov, V. B. Prakapenka, E. Edmund, S. Chariton, Z. Konôpková, C. Strohm, C. Sanchez-Valle, M. Frost, L. Andriambariariaona, K. Appel, C. Baehtz, O. B. Ball, R. Briggs, J. Buchen, V. Cerantola, J. Choi, A. L. Coleman, H. Cynn, A. Dwivedi, H. Graafsma, H. Hwang, E. Koemets, T. Laurus, Y. Lee, X. Li, H. Marquardt, A. Mondal, M. Nakatsutsumi, S. Ninet, E. Pace, C. Pepin, C. Prescher, S. Stern, J. Sztuk-Dambietz, U. Zastrau, M. I. McMahon, Phase transition kinetics of superionic H₂O ice phases revealed by Megahertz X-ray free-electron laser-heating experiments. *Nat. Commun.* 15, 8256 (2024).
28. E. Sugimura, T. Komabayashi, K. Ohta, K. Hirose, Y. Ohishi, L. S. Dubrovinsky, Experimental evidence of superionic conduction in H₂O ice. *J. Chem. Phys.* 137, 194505 (2012).
29. F. Grasselli, L. Stixrude, S. Baroni, Heat and charge transport in H₂O at ice-giant conditions from ab initio molecular dynamics simulations. *Nat. Commun.* 11, 3605 (2020).
30. L. Stixrude, S. Baroni, F. Grasselli, Thermal and tidal evolution of Uranus with a growing frozen core. *Planet. Sci. J.* 2, 222 (2021).
31. H. Wang, U. Ail, R. Gabrielsson, M. Berggren, X. Crispin, Ionic Seebeck Effect in Conducting Polymers. *Adv. Energy Mater.* 5, 1500044 (2015).

32. C. G. Han, X. Qian, Q. Li, B. Deng, Y. Zhu, Z. Han, W. Zhang, W. Wang, S. P. Feng, G. Chen, W. Liu, Giant thermopower of ionic gelatin near room temperature. *Science* 368, 1091–1098 (2020).
33. C. Chi, M. An, X. Qi, Y. Li, R. Zhang, G. Liu, C. Lin, H. Huang, H. Dang, B. Demir, Y. Wang, W. Ma, B. Huang, X. Zhang, Selectively tuning ionic thermopower in all-solid-state flexible polymer composites for thermal sensing. *Nat. Commun.* 13, 221 (2022).
34. N. Jabeen, M. Muddasar, N. Menéndez, M. A. Nasiri, C. M. Gómez, M. N. Collins, R. Muñoz-Espí, A. Cantarero, M. Culebras, Recent advances in ionic thermoelectric systems and theoretical modelling. *Chem. Sci.* 15, 14122–14153 (2024).
35. O. Nickel, L. J. V. Ahrens-Iwers, R. H. Meißner, M. Janssen, Water, not salt, causes most of the Seebeck effect of nonisothermal aqueous electrolytes. *Phys. Rev. Lett.* 132, 186201 (2024).
36. X. Qian, Z. Ma, Q. Huang, H. Jiang, R. Yang, Thermodynamics of ionic thermoelectrics for low-grade heat harvesting. *ACS Energy Lett.* 9, 679–706 (2024).
37. A. Forestier, G. Weck, F. Datchi, S. Ninet, G. Garbarino, M. Mezouar, P. Loubeyre, X-ray signature of the superionic transition in warm dense fcc water ice. *Phys. Rev. Lett.* 134, 076102 (2025).
38. M. French, M. P. Desjarlais, R. Redmer, Ab initio calculation of thermodynamic potentials and entropies for superionic water. *Phys. Rev. E* 93, 022140 (2016).
39. N. I. Pavlenko, I. V. Stasyuk, The effect of proton interactions on the conductivity behavior in systems with superionic phases. *J. Chem. Phys.* 114, 4607–4617 (2001).
40. N. Nettelmann, R. Helled, J. J. Fortney, R. Redmer, New indication for a dichotomy in the interior structure of Uranus and Neptune from the application of modified shape and rotation data. *Planet. Space Sci.* 77, 143–151 (2013).
41. A. Sohn, C. Yu, Ionic transport properties and their empirical correlations for thermal-to-electrical energy conversion. *Mater. Today Phys.* 19, 100433 (2021).
42. S. Sun, M. Li, X. L. Shi, Z. G. Chen, Advances in ionic thermoelectrics: from materials to devices. *Adv. Energy Mater.* 13, 2203692 (2023).
43. A. C. Mitchell, W. J. Nellis, Equation of state and electrical conductivity of water and ammonia shocked to the 100 GPa (1 Mbar) pressure range. *J. Chem. Phys.* 76, 6273–6281 (1982).
44. K. Oka, Y. Okuda, K. Hirose, Hot interiors of ice giant planets inferred from electrical conductivity of dense H₂O fluid. *arXiv preprint arXiv*, 2401.11454, (2024).
45. B. Militzer, Ab Initio Entropy Calculations of Water Predict the Interiors of Uranus and Neptune to Be 15%–30% Colder than Previous Models. *Astrophys. J.* 990, 20 (2025).
46. S. Markham, D. Stevenson, Constraining the effect of convective inhibition on the thermal evolution of Uranus and Neptune. *Planet. Sci. J.* 2, 146 (2021).
47. N. Nettelmann, K. Wang, J. J. Fortney, S. Hamel, S. Yellamilli, M. Bethkenhagen, R. Redmer, Uranus evolution models with simple thermal boundary layers. *Icarus* 275, 107–116 (2016).

48. M. Podolak, R. Helled, G. Schubert, Effect of non-adiabatic thermal profiles on the inferred compositions of Uranus and Neptune. *Mon. Not. R. Astron. Soc.* 487, 2653–2664 (2019).
49. L. Scheibe, N. Nettelmann, R. Redmer, Thermal evolution of Uranus and Neptune-II. Deep thermal boundary layer. *Astron. Astrophys.* 650, A200 (2021).
50. H. Ravit, N. Nadine, G. Tristan, Uranus and Neptune: Origin, Evolution and Internal Structure. *Space Sci. Rev.* 216, 38 (2020).
51. A. N. Dmitriev, Thermoelectric Currents of Earth’s Core Generate the Earth’s Magnetic Field. *Int. J. Geosci.* 8, 1048–1071 (2017).
52. S. Pan, T. Huang, A. Vazan, Z. Liang, C. Liu, J. Wang, C. J. Pickard, H. T. Wang, D. Xing, J. Sun, Magnesium oxide-water compounds at megabar pressure and implications on planetary interiors. *Nat. Commun.* 14, 1165 (2023).
53. H. Gao, C. Liu, J. Shi, S. Pan, T. Huang, X. Lu, H. -T. Wang, D. Xing, J. Sun, Superionic Silica-Water and Silica-Hydrogen Compounds in the Deep Interiors of Uranus and Neptune. *Phys. Rev. Lett.* 128, 035702 (2022).

Acknowledgments: Numerical computations were supported by the Open Source Supercomputing Center of S-A-I. **Funding:** The project is supported by National Key Research and Development Program of China, Grant No. 2024YFF0807500 (to Y.H.). We acknowledge the support of the National Natural Science Foundation of China, 42350002 (to Y.H.), the CAS Youth Interdisciplinary Team, JCTD-2022-16 (to Y.H.). **Author contributions:** Conceptualization: Y.H., Methodology: D.L., Z.W., Y.H., S.Y. Investigation: D.L., Y.H. Visualization: D.L., C.Z. Funding acquisition: Y.H. Supervision: Y.H. Writing—original draft: D.L., Y.H. Writing—review & editing: D.L., Z.W., Y.H., G.X., C.Z., S.Y. **Competing interests:** The authors declare that they have no competing interests. **Data and materials availability:** Data needed to evaluate the conclusions in the paper are present in the paper and/or the Supplementary Materials.

Supplementary Materials

Methods

Figs. S1 to S21

Tables S1 to S2

References (54–88)

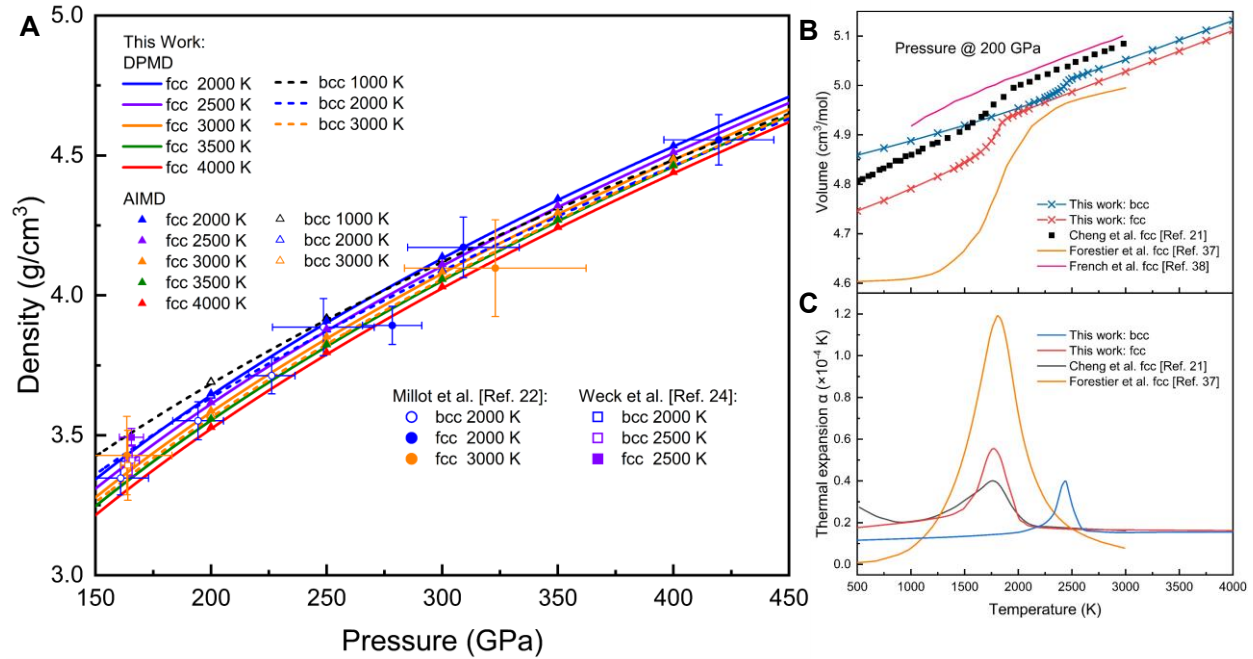


Fig. 1. Thermodynamic properties of bcc and fcc H₂O at 150–450 GPa and 2000–4000 K. (A) Density-pressure relationships of the bcc and fcc H₂O at high *P-T*. The colors of the curves and symbols correspond to the magnitude of temperature along isotherms. Dashed and solid curves represent the DPMG calculation results for the bcc and fcc phases, respectively. Open and solid triangle symbols represent the AIMD calculation results. The previous experimental results are noted with circles (22) and squares (24). (B) Calculated molar volumes of bcc (blue cross-dotted line) and fcc (red cross-dotted line) are presented as a function of temperature along isobar at 200 GPa. A sharpening of the change in molar volume with increasing temperature suggests SI transition (21, 37, 38). (C) The volumetric thermal expansion coefficients are represented by blue and red curves for bcc and fcc H₂O in comparison with previous results (20, 36)

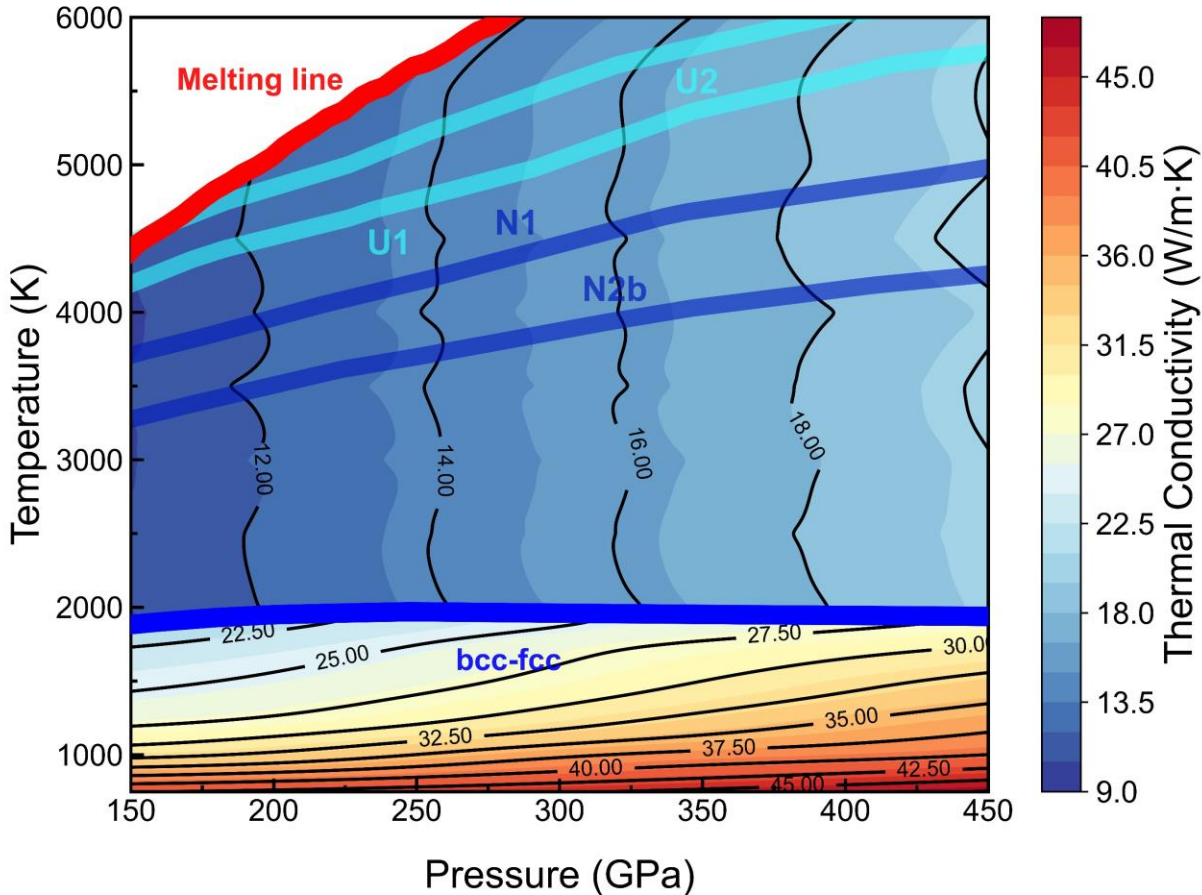


Fig. 2. Thermal conductivities of bcc and fcc H₂O under conditions relevant to the interiors of Uranus and Neptune. The contour lines indicate the magnitude of thermal conductivities. The blue and red curves exhibit the bcc-to-fcc and fcc-to-liquid phase boundary (37), respectively. The cyan shaded band represents the U1 and U2 models, corresponding to the thermal profile of Uranus's interior (40). The dark blue shaded band represents the N1 and N2b models, corresponding to the thermal profile of Neptune's interior (40).

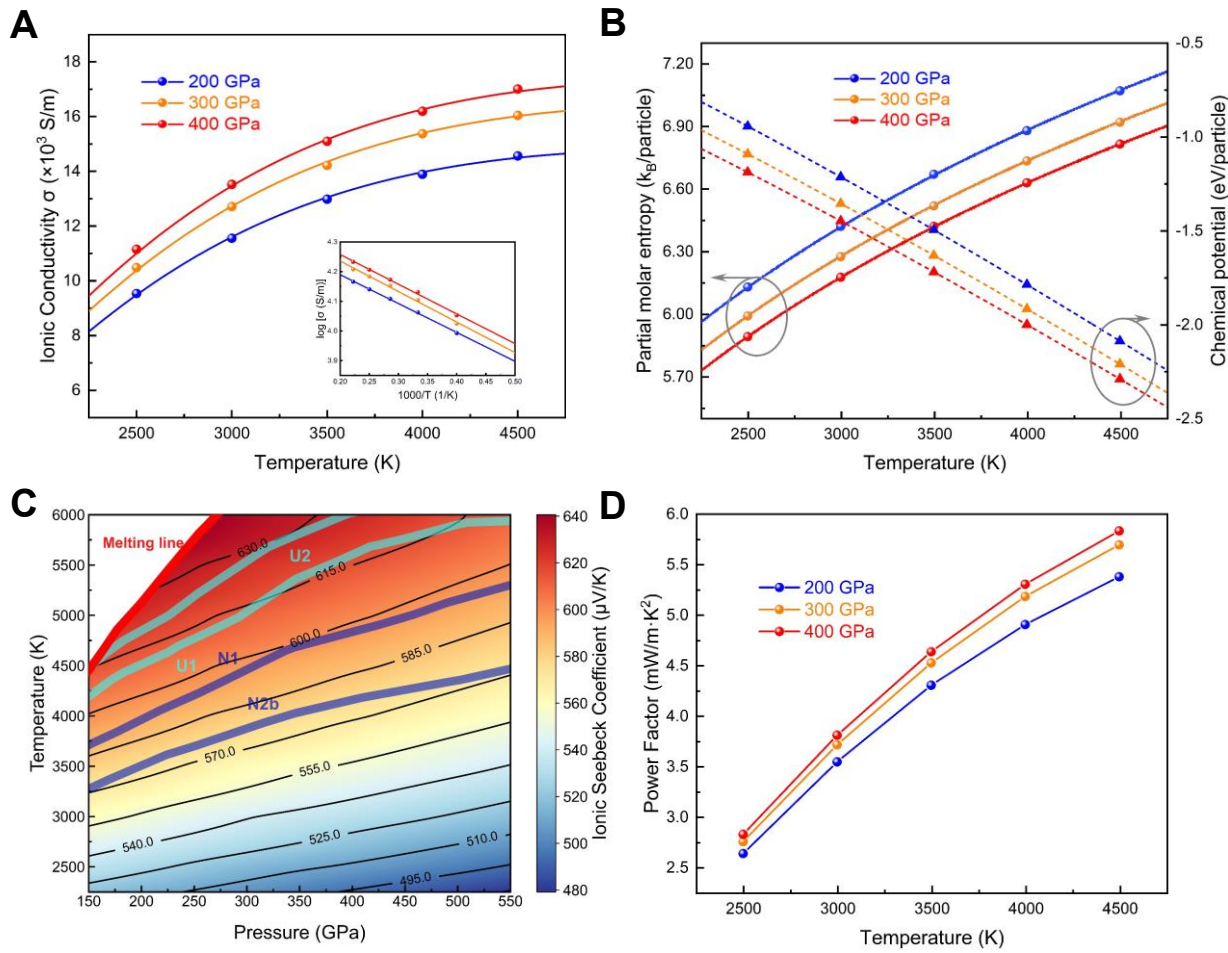


Fig. 3. Protonic Thermoelectric and transport properties of fcc SI H₂O ice under conditions relevant to the interiors of Uranus and Neptune. (A) Ionic conductivities of fcc H₂O with increasing temperature at 200 GPa, 300 GPa, and 400 GPa. The inset shows the logarithmic representation of conductivities for Arrhenius equation. (B) Temperature dependence of the partial molar entropy (solid lines) and chemical potential (dashed lines) for proton at 200–400 GPa. (C) Contour map of the proton Seebeck coefficient as a function of pressure and temperature of planetary thermal profiles (U1, U2 for Uranus and N1, N2b for Neptune) (40) and the melting curve highlighted (37). (D) Ionic power factor as a function of temperature at 200–400 GPa.

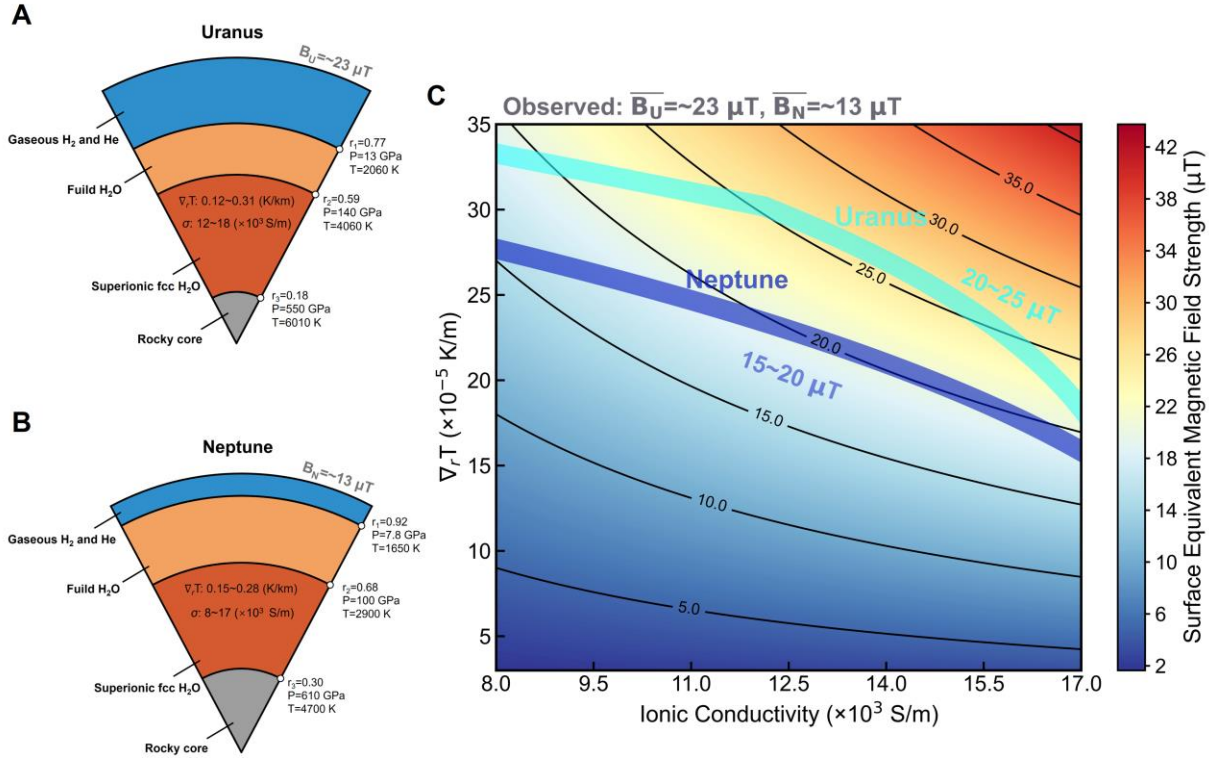


Fig. 4. The thermodynamic profiles of ice giants and the dependence of surface-equivalent magnetic field strength on ionic conductivity and temperature gradient. (A) Uranus' and (B) Neptune's thermodynamic profiles of interior structures. (C) Contour map of the surface-equivalent magnetic strength as a function of ionic conductivity and radial temperature gradient for a fixed thermoelectric conversion efficiency of $\eta=2.5\%$. The cyan and dark blue shaded bands highlight the predicted surface magnetic field strength based on the ionic conductivity and temperature gradient parameters of Uranus and Neptune. These regions present great consistence with the observed surface-equivalent magnetic field strength of Uranus ($\bar{B}_U \approx 23 \mu\text{T}$) (2) and Neptune ($\bar{B}_N \approx 13 \mu\text{T}$) (3).

Supplementary Materials for

Protonic thermoelectric effect of Superionic H₂O and magnetic field generation in Uranus and Neptune

Daohong Liu^{1,2}, Wei Zhang³, Yu He^{1,4,5*}, Xinzhan Guo¹, Chuanyu Zhang⁶, Yang Sun⁷

¹State Key Laboratory of Critical Mineral Research and Exploration, Institute of Geochemistry, Chinese Academy of Sciences, Guiyang 550081, China.

²College of Earth and Planetary Sciences, University of Chinese Academy of Sciences, Beijing 100049, China.

³School of Geography and Environmental Science (School of Karst Science), Guizhou Normal University, Guiyang 550025, China.

⁴Key Laboratory of High-Temperature and High-Pressure Study of the Earth's Interior, Institute of Geochemistry, Chinese Academy of Sciences, Guiyang 550081, Guizhou, China

⁵Center for High Pressure Science and Technology Advanced Research, Shanghai 201203, China.

⁶College of Physics, Chengdu University of Technology, Chengdu, 610059, China.

⁷School of Materials, Sun Yat-sen University, Shenzhen, China.

*Corresponding author: heyu@mail.gyig.ac.cn

The PDF file includes:

Methods

Figs. S1 to S21

Tables S1 to S2

References

Methods

DFT-MD Calculations

All ab initio molecular dynamics (AIMD) simulations of bcc and fcc H₂O under extreme conditions were performed within the framework of Kohn-Sham Density Functional Theory (KS-DFT) (54, 55). The calculations were executed with the open-source software packages ABACUS (v3.8.4) (56–58), in which the exchange-correlation energy was described by the Perdew-Burke-Ernzerhof (PBE) functional within the generalized gradient approximation (GGA) (59), augmented by Grimme's D3 dispersion correction (60). The electronic states were represented by SG15 Optimized Norm-Conserving Vanderbilt (SG15-ONCV) pseudopotentials (61), in combination with a Linear Combination of Atomic Orbitals (LCAO) basis set of double-zeta plus polarization (DZP) numerical atomic orbitals (62).

We employed periodic simulation cells with 54 and 32 water molecules for bcc and fcc phase, respectively (21, 22, 25). To reproduce the targeted thermodynamic regime, lattice parameters were systematically adjusted so that trajectories could be generated across 100–500 GPa and 1000–5000 K conditions within the canonical (*NVT*) ensemble at a timestep of 0.5 fs, and initial training databases for neural network model were generated by randomly sampling representative snapshots from the trajectories.

For all simulations, the kinetic energy cutoff was set to 100 Ry, while the self-consistent field (SCF) convergence threshold was 10^{−6} Ry in total electronic energy. Additionally, K-spacing was 0.2 to ensure reliable convergence of both energies and atomic forces.

Construction of Deep Potential Model

The machine-learning interatomic potential was constructed within the deep potential (DP) framework using the descriptor “se_e2_a” (63, 64), as implemented in the DeePMD-kit package (v2.2.8) (65–67). The training databases were generated by using an active-learning workflow employing the DP-GEN package, in which candidate configurations were iteratively explored and gained (68). The procedure was performed across a wide range thermodynamic conditions, spanning 100–500 GPa and 1000–5000 K, with atomic energies, forces and stresses computed at each iteration, resulting in 4,877 configurations were collected for training and 300 configurations were reserved for testing in total. A cutoff radius of 6 Å, which was smoothly decayed to 0.5 Å with 1/r function, was employed during the DP-GEN iterations to alleviate discontinuities at the cutoff boundary. The neural network framework that was used for this

model comprised embedding layers of sizes {25, 50, 100} and fitting layers of sizes {240, 240, 240}.

The initial bcc and fcc training sets for active learning workflow in DP-GEN were generated by using ABACUS-AIMD simulations. Figs. S1 and S2 illustrate the corresponding trajectories of both phases at 200 GPa across 1000–2000K and 2000–4000 K. During the iterative dataset exploration, configurations selected for labeling were constrained within a predefined force deviation trust interval, denoted as ε_{low} and $\varepsilon_{\text{high}}$. For the lower temperature iteration (1000–2500 K) group, where atomic forces along the trajectories exhibited modest fluctuations, the ε_{low} and $\varepsilon_{\text{high}}$ were set to 0.20 and 0.35 eV/Å, respectively. For the higher temperature iteration (3000–5000 K) group, where the atomic force fluctuations became more pronounced, and the corresponding ε_{low} and $\varepsilon_{\text{high}}$ were modified to 0.30 and 0.50 eV/Å, respectively. Finally, for both group, DP-GEN achieved labeling accuracy exceeding 96% for all visited configurations, with labeling failure rates below 3%, demonstrating that the thermodynamic phase space was fully explored.

To optimize the training process, the Adam stochastic gradient descent algorithm was employed (69), in which the learning rate was exponentially decreased from 1×10^{-3} to 3.51×10^{-8} over 5000 decay steps. The prefactors in the loss function are utilized to control the influence of different physical quantities. The prefactors of the energy term, the force term, and the virial term are set from 0.2 to 1, 1000 to 1, and 0.2 to 1, respectively. In the final stage of training, a cutoff radius of 8.0 Å was implemented to capture long-range interactions, with the maximum neighbors of 395 and 796 for O and H atoms, respectively.

The optimized DP model was subsequently validated by using independent datasets. The absolute prediction errors reached 8.606 meV/atom for energies, 333.7 meV/Å for forces, 1.972 GPa for pressures, and 1.035 GPa for shear stresses. Comparisons between DP and AIMD calculations are provided in Fig. S3, while the agreement between radial distribution functions (RDFs) obtained from deep potential molecular dynamic (DPMD) and AIMD simulations is shown in Fig. S4 and Fig. S5, also confirming that the DP model had achieved convergence.

DPMD Calculations

All DPMD calculations of bcc and fcc H₂O were performed by using the Large-scale Atomic/Molecular Massively Parallel Simulator (LAMMPS) package, which was interfaced with the DP module (70–72). Throughout the simulations, the system temperature and pressure were

controlled by Langevin thermostat and Nosé-Hoover barostat with the damping parameters of 50 and 500 fs, respectively (73). Additionally, a 0.5 fs time step was selected for integration of the equations of motion to preserve the stability of the atomic trajectories over the simulations.

Lattice Thermal Conductivity

The lattice thermal conductivity of bcc and fcc phases was computed using the non-equilibrium molecular dynamics (NEMD) based on the Müller-Plathe (MP) method as implemented within the DPMD framework (74–78). According to Fourier's law of heat conduction, the thermal conductivity κ is expressed as:

$$\kappa = -\frac{\langle J_z(t) \rangle}{\langle \partial T / \partial z \rangle} \quad (6)$$

where the time average of the heat flux is denoted as $\langle J_z(t) \rangle$, and the time average of the temperature gradient in the simulation cell is represented as $\langle \partial T / \partial z \rangle$.

In the MP framework, the heat flux is constructed by periodically exchanging the velocities of atoms between two predefined regions, referred to as the "hot region" and the "cold region", which are placed symmetrically within the simulation cell. At a fixed interval, the hottest atom in the "cold region" and the coldest atom in the "hot region" are selected, and their velocities are exchanged according to

$$v'_c = -v_c + 2 \frac{m_c v_c + m_h v_h}{m_c + m_h} \quad (7)$$

$$v'_h = -v_h + 2 \frac{m_c v_c + m_h v_h}{m_c + m_h} \quad (8)$$

in which the atomic masses m_c and m_h , along with their initial velocities v_c and v_h , are used in the energy exchange, which induces a controlled heat flux while ensuring that the total energy of the system is conserved. Therefore, the lattice thermal conductivity expression in Eq. (6) will be modified as follows:

$$\kappa = -\frac{\sum_{\text{transfers}} \frac{1}{2} m (v_h^2 - v_c^2)}{2t L_x L_y \langle \partial T / \partial z \rangle} \quad (9)$$

where t represents the total effective duration over the NEMD simulation, and L_x and L_y were corresponding to the lengths of the simulation cell along the x and y directions, respectively.

To eliminate boundary scattering caused by finite-size effects, a series of simulations were performed with different lengths L_z along the heat flux direction, while maintaining constant

cross-sectional L_x and L_y sizes. The extrapolation to the infinite size was conducted by fitting the inverse thermal conductivity to the inverse length (79):

$$\frac{1}{\kappa(L)} = \frac{1}{\kappa_\infty} \left(1 + \frac{\lambda}{L} \right) \quad (10)$$

where the lattice thermal conductivity $\kappa(L)$ is the cells length L along the heat transfer direction, while κ_∞ represents the lattice thermal conductivity of a theoretically infinite cells length, also, the reciprocal of κ_∞ is the intercept of the linear fitting.

NEMD simulations were performed using the LAMMPS package and the initial configurations were equilibrated within the NVT ensemble for 200 ps using a Nosé-Hoover thermostat to achieve the target temperature. Subsequently, the simulation system was switched to the NVE ensemble, and a steady heat flux was imposed by exchanging kinetic energy between the hot and cold reservoirs separated by a fixed distance along the transport direction. The simulation was conducted with a time step of 0.5 fs, and the system was allowed to reach steady-state thermal transport over 0.5 ns, and the followed 1.0 ns simulation was used to collect data of temperature gradient.

As shown in Fig. S6, bcc H₂O ice exhibits a nonlinear regime, the extent of which progressively diminishes as the temperature increases. In contrast, fcc H₂O ice maintains a consistently linear temperature gradient across the entirely investigated temperature range.

To further illustrate the convergence behavior of the temperature gradient, we averaged the instantaneous temperature gradient over the entire simulation trajectory, thereby generating a time-resolved profile that reveals the evolution of the gradient as a function of simulation time (Fig. S7). It was observed that, as the simulation progressed, the temperature gradient gradually approached convergence and achieved a steady state at approximately 0.5 ns.

Due to the influence of boundary scattering, NEMD calculations were susceptible to a finite-size effect, which manifested as an increase in thermal conductivity with an enlargement of the simulation cells. Therefore, to extrapolate the lattice thermal conductivity, a correction was determined by using linear relationship between the inverse of the thermal conductivity and the inverse of the simulation cell size, as depicted in Fig. S8. As shown in Fig. S9, the thermal conductivity exhibits pronounced difference across solid-SI transitions, reflecting the relationship between ionic mobility and heat conduction mechanisms.

Diffusion Coefficient and Ionic Conductivity

The ionic transport properties were investigated by employing DPMD simulations, in which the mean square displacements (MSDs) method was used to calculate the diffusion coefficients of the species (74, 75). The simulations were executed in the *NVT* ensemble with a time step of 0.5 fs, where the temperature was controlled by a Langevin thermostat to ensure accurate sampling of the particle distribution. The MSDs of each ionic species can be computed as:

$$MSD(t) = \frac{1}{N} \sum_{i=1}^N \langle |\vec{r}_i(t) - \vec{r}_i(0)|^2 \rangle \quad (2)$$

where N is the number of target ions, and $\vec{r}_i(t)$ represents the position of the i -th ion at time t . The diffusion coefficient D was then obtained from the long-time linear regime of the MSDs according to the Einstein relation,

$$D = \frac{1}{2d} \frac{d}{dt} (MSD(t)) \quad (3)$$

where d is the dimensionality of the system. The diffusion coefficients calculated at various temperatures were fitted with an Arrhenius equation:

$$D(T) = D_0 \exp\left(-\frac{\Delta H}{k_B T}\right) \quad (4)$$

where ΔH is the activation enthalpy, D_0 is a pre-exponential factor, k_B is the Boltzmann constant, and T is the temperature. Based on the diffusion coefficients, the ionic conductivity σ was estimated via the Nernst-Einstein equation,

$$\sigma_i(T) = \frac{fn_i q_i^2}{k_B T} D_i(T) \quad (5)$$

in which n_i denotes the number density of transport ions, q_i is their charge.

Based on the DP model, the bulk self-diffusion properties of bcc and fcc H₂O ice were calculated using DPMD. To investigate the diffusion properties within the corresponding temperature and pressure ranges, a Langevin thermostat and a Nosé-Hoover barostat were employed to control the temperature and pressure of the system, respectively, and a 0.5 fs time step was used to integrate the equations of motion. For the bcc and fcc phases, supercells of 10 × 10 × 10 and 8 × 8 × 8, which contain 6000 and 6144 atoms respectively, were used to converge the calculation results and reduce the impact from size effect. The simulation cell volume was determined by performing a 30 ps simulation under the *NPT* ensemble, wherein the initial 10 ps served as a pre-equilibration stage. The averaged cell sizes under the targeted pressure-temperature conditions were extracted from this trajectory. Subsequently, the *NVT* ensemble was

subjected to DPMD simulations for bcc and fcc under the thermodynamic conditions of 200–400 GPa, 1000–2000 K and 2500–4500 K for up to 50 ps to obtain the respective MSDs, as shown in Figs. S10 and S11.

The MSDs of both bcc and fcc phases ice exhibit a progressive increase with temperature, indicating enhanced proton mobility. Notably, when the temperature approaches 1750 K, protons within bcc ice commence diffusion and gradually undergo a superionic transition, whereas the MSDs of protons in the fcc phase exhibit a more uniform temperature dependence and remain largely insensitive to pressure variations. On this basis, the diffusion coefficient of proton for fcc H₂O was subsequently calculated, as presented in Fig. S12. In agreement with the behavior of MSDs illustrated in Fig. S11, the logarithm of the diffusion coefficient demonstrates a distinct linear correlation with the reciprocal temperature, while showing negligible dependence on pressure.

Ionic Thermodiffusion Effect to Thermopower

All calculations of ionic thermoelectric effects in SI fcc phase are performed within the framework of Onsager relations (32, 80, 81). In the electrolyte system, the ionic flux is finally determined as (81–83):

$$J_i = -D_i \left(\frac{\partial n_i}{\partial z} + \frac{q_i n_i}{k_B T} E_z + \frac{n_i}{k_B T} \frac{\partial \mu_i}{\partial z} \right) \quad (11)$$

where E_z represents the hypothetical thermoelectric field and μ_i represents the chemical potential of i -species. The relationship between the chemical potential of the i -species and the temperature gradient is expressed as follows (83, 84):

$$\frac{\partial \mu_i}{\partial z} = \frac{\partial \mu_i}{\partial T} \cdot \frac{\partial T}{\partial z} \quad (12)$$

At steady state, the current in the circuit is zero, then:

$$\sum_i q_i J_i = 0 \quad (13)$$

$$-\sum_i D_i \cdot \left(q_i \nabla n_i + \frac{q_i^2 n_i}{k_B T} \nabla V + \frac{q_i \hat{S}_i n_i}{k_B T} \nabla T \right) = 0 \quad (14)$$

Generally, when the ion concentration gradient is negligible,

$$\sum_i \left(\frac{q_i^2 n_i D_i}{k_B T} E_z + \frac{q_i n_i \hat{S}_i D_i}{k_B T} \frac{\partial T}{\partial z} \right) = 0 \quad (15)$$

$$E_z = - \frac{\sum_i q_i n_i \widehat{S}_i D_i}{\sum_i q_i^2 n_i D_i} \frac{\partial T}{\partial z} \quad (16)$$

In the SI fcc phase, O atoms occupy the sublattice sites, leading to its diffusion coefficient $D_O \approx 0$ so that the **Eq. (16)** is further modified to

$$\frac{\partial V}{\partial z} = - \frac{\widehat{S}_H}{q_H} \frac{\partial T}{\partial z} \quad (17)$$

Therefore, the ionic thermoelectric coefficient of SI fcc, namely the Seebeck coefficient, can be calculated according to **Eq. (17)**.

In addition, the chemical potential is calculated by employing the Widom insertion method (85),

$$\mu_i = k_B T \ln(\rho_i \lambda^3) - k_B T \ln \left(\langle \exp \left(-\frac{\psi_i}{k_B T} \right) \rangle \right) \quad (18)$$

where ρ_i is the number density of the i -species and ψ_i is the interaction energy of the inserted particle (single) with all other particles in the system.

Calculations of Magnetic Field for Icy Mantles

To evaluate the contribution of thermoelectrically driven currents within the superionic ice shell to the planetary-scale magnetic field, a mathematical framework for calculating the magnetic field generated by thermoelectric effects was established in spherical coordinates. The superionic ice layer was treated as a spherical shell with an outer radius R_{SI} , across which a temperature gradient was assumed to exist in the radial direction. Therefore, the charge-continuity equation in spherical coordinates can be written as:

$$\nabla \cdot \vec{J} + \frac{\partial \rho}{\partial t} = 0 \quad (19)$$

where the ρ is the charge density and \vec{J} is the current density vector. On a planetary scale, it is assumed that the charge within the superionic ice layer does not change with time, i.e.:

$$\frac{\partial \rho}{\partial t} = 0 \quad (20)$$

Finally, the current density vector in spherical coordinates can be expressed as:

$$\frac{1}{r^2} \frac{\partial}{\partial r} (r^2 J_r) + \frac{1}{r \sin \theta} \frac{\partial}{\partial \theta} (\sin \theta J_\theta) + \frac{1}{r \sin \theta} \frac{\partial J_\phi}{\partial \phi} = 0 \quad (21)$$

To simplify the derivation, we assumed that the current density is axisymmetric along the ϕ direction, i.e., $\partial J_\phi / \partial \phi = 0$. Under this condition, the J_θ component is decoupled from the

governing equations and can therefore be expressed solely as a function of r and θ , i.e., $J_\theta = J_\theta(r, \theta)$, which is independent of the φ component.

Furthermore, since the system exhibits an average axisymmetric distribution, its azimuthal component can be approximated by the radial component, and based on geometric projection relationships, it is assumed that (51):

$$J_\phi = J_\phi(r, \theta) \approx J_r \sin \theta \quad (22)$$

This approximation describes the azimuthal current induced by the deflection of charge carriers along an isothermal spherical shell. The radial current itself is determined by the thermoelectric effect (86):

$$J_r = \sigma S \frac{\partial T}{\partial r} \quad (23)$$

where S , σ and $\frac{\partial T}{\partial r}$ are the thermopower, ionic conductivity, and radial temperature gradient, respectively.

To further simplify the calculations, the spherical shell current model is equivalent to a magnetic dipole moment model, and then the planetary magnetic field generated by the superionic ice layer is calculated. Therefore, the magnetic moment generated by the current density in the superionic ice layer can be expressed as:

$$\vec{m} = \frac{1}{2} \int_V \vec{r}' \times \vec{J}(\vec{r}') dV' = \frac{1}{2} \int_V \vec{r}' \times (J_r' \vec{e}_{r'} + J_\theta' \vec{e}_\theta' + J_\varphi' \vec{e}_\varphi') dV' \quad (24)$$

Furthermore, it can be expanded as:

$$m_x = -\frac{1}{2} \int_{r_{in}}^{r_{out}} \int_0^\pi \int_0^{2\pi} r'^3 (J_\theta \sin \varphi + J_\varphi(r', \theta) \cos \theta \cos \varphi) \sin \theta d\varphi d\theta dr' \quad (25)$$

$$m_y = -\frac{1}{2} \int_{r_{in}}^{r_{out}} \int_0^\pi \int_0^{2\pi} r'^3 (-J_\theta \cos \varphi + J_\varphi(r', \theta) \cos \theta \sin \varphi) \sin \theta d\varphi d\theta dr' \quad (26)$$

$$m_z = +\frac{1}{2} \int_{r_{in}}^{r_{out}} \int_0^\pi \int_0^{2\pi} r'^3 J_\varphi(r', \theta) \sin^2 \theta d\varphi d\theta dr' \quad (27)$$

Considering spherical symmetry, the expression for the magnetic moment component can be further simplified to:

$$\int_0^{2\pi} \cos \varphi d\varphi = \int_0^{2\pi} \sin \varphi d\varphi = 0 \quad (28)$$

$$m_x = m_y = 0 \quad (29)$$

$$m_z \approx \frac{1}{2} R_{SI}^3 \int_{r_{in}}^{r_{out}} \int_0^\pi \int_0^{2\pi} J_\phi(r', \theta) \sin^2 \theta d\phi d\theta dr' \quad (30)$$

Thus, according to the Biot-Savart law, the differential form of the surface magnetic field of a planet can be expressed as:

$$dB(\vec{r}) = \frac{\mu_0}{4\pi} \frac{\vec{J} \times \vec{R}}{R^3} dV' \quad (31)$$

Within the framework of the dipole approximation, the magnetic flux density can finally be calculated as:

$$B(\vec{r}) \approx \frac{\mu_0}{4\pi R^3} (3\vec{e}_r(\vec{m} \cdot \vec{e}_r) - \vec{m}) \quad (32)$$

where μ_0 is permeability of free space and R represents planetary radius. Based on the Eq. (31), the components of the magnetic flux density can be further expressed as:

$$B_r(r, \theta) = \frac{\mu_0}{4\pi} \frac{2m_z \cos \theta}{r^3} \quad (33)$$

$$B_\theta(r, \theta) = \frac{\mu_0}{4\pi} \frac{m_z \sin \theta}{r^3} \quad (34)$$

Efficiency Evaluation of *i*-TE and its Constraint on Current Density

Thermal transport property is a significant aspect for *i*-TE materials because the thermal-to-electric conversion performance is based on the establishment of temperature differences. However, in real systems, current power cannot violate the law of conservation of energy. Therefore, we introduce thermoelectric conversion efficiency to constrain the relationship between the maximum sustainable heat flow and thermoelectric current power.

The local thermoelectric power density, defined as the electrical power generated per unit volume during the thermoelectric process, can be given by the dot product of the electric current and the electric field:

$$p_{elec}(r) = \vec{J} \cdot \vec{E} \quad (35)$$

It can be integrated along the shell thickness to approximate the electrical power output per unit area through a thickness R_{SI} :

$$P_{elec/area} \approx p_{elec} R_{SI} = \sigma S^2 (\nabla T)^2 R_{SI} \quad (36)$$

The available heat flux, which can be derived from thermal conductivity, is the magnitude of the heat flux under Fourier's law:

$$|Q_{heat}| = \kappa |\nabla T| \quad (37)$$

Thus, the energy constraint can be expressed as:

$$P_{\text{elec/area}} \leq \eta_{\text{max}} |q_{\text{heat}}| \quad (38)$$

where η_{max} is the thermoelectric conversion efficiency. It can be calculated by using the following formula (31, 87, 88):

$$zT = \frac{S^2 \sigma T}{\kappa} \quad (39)$$

$$\eta_{\text{max}} = \frac{T_H - T_C}{T_H} \frac{\sqrt{zT + 1} - 1}{\sqrt{zT + 1} + T_C/T_H} \quad (40)$$

in which the zT , T_H and T_C are thermoelectric figure of merit, hot end temperature and cold end temperature, respectively.

Based on **Eq. (38)**, an inequality is obtained, which further constrains the maximum value of the current density.

$$J_r^{\text{max}} \leq \frac{\eta_{\text{max}} \kappa}{S R_{SI}} \quad (41)$$

And finally, the maximum conversion efficiency calculated based on the above relationship at different pressures and temperatures, and the radial thermoelectric current density inside Uranus and Neptune at different conversion efficiencies, are shown in Fig. S13.

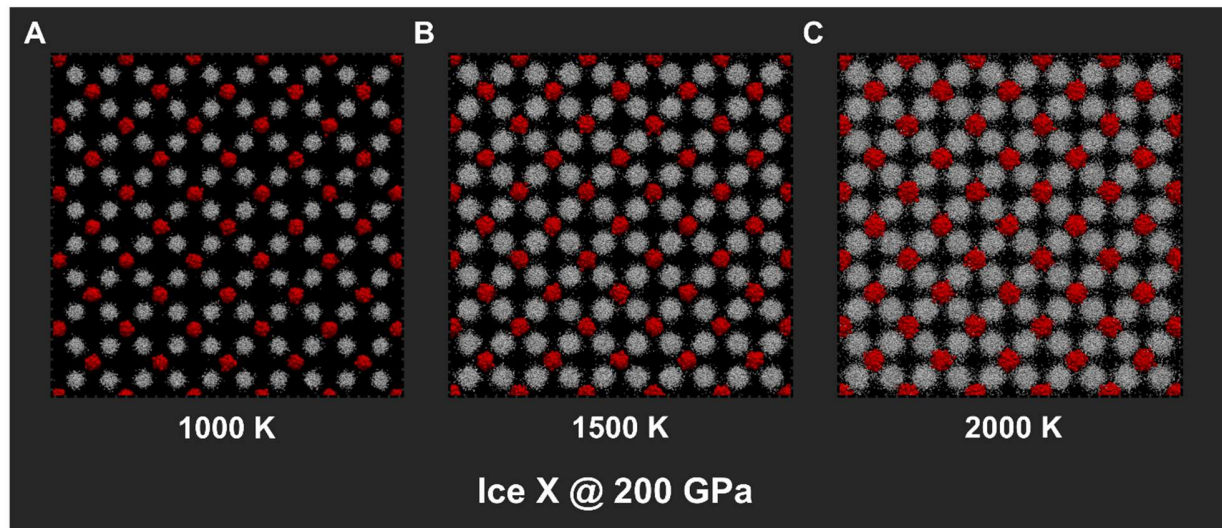


Fig. S1. Multi-frames trajectories of bcc H₂O at 200 GPa and 1000–2000 K obtained from molecular dynamics simulations. Snapshots of (A) 1000 K, (B) 1500 K, and (C) 2000 K are presented. The red and white spheres represent O and H atoms, respectively.

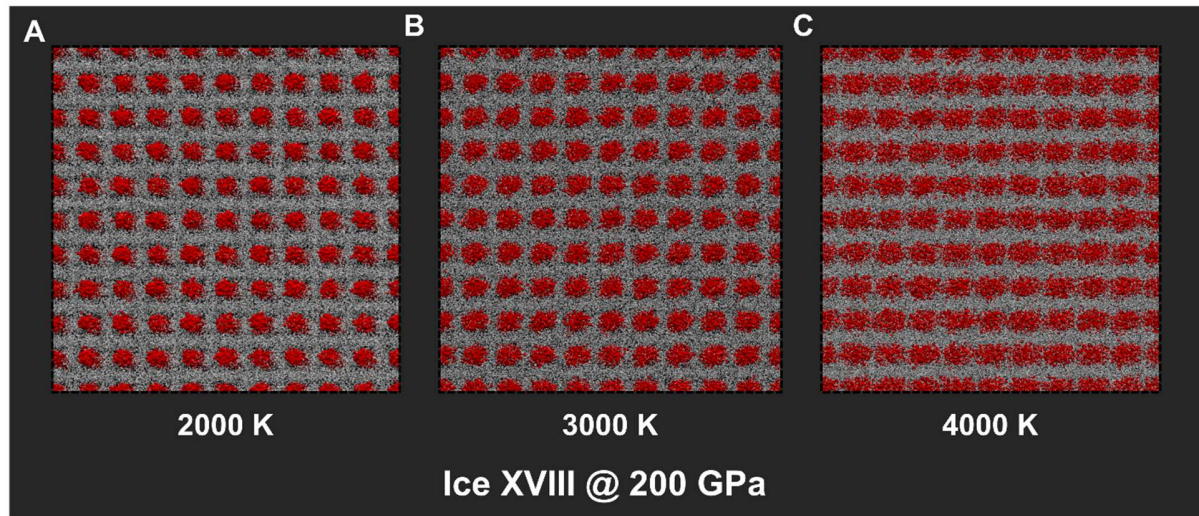


Fig. S2. Multi-frames trajectories of fcc H₂O at 200 GPa and 2000–4000 K obtained from molecular dynamics simulations. Snapshots of (A) 2000K, (B) 3000K, and (C) 4000K are presented. The red and white spheres represent O and H atoms, respectively.

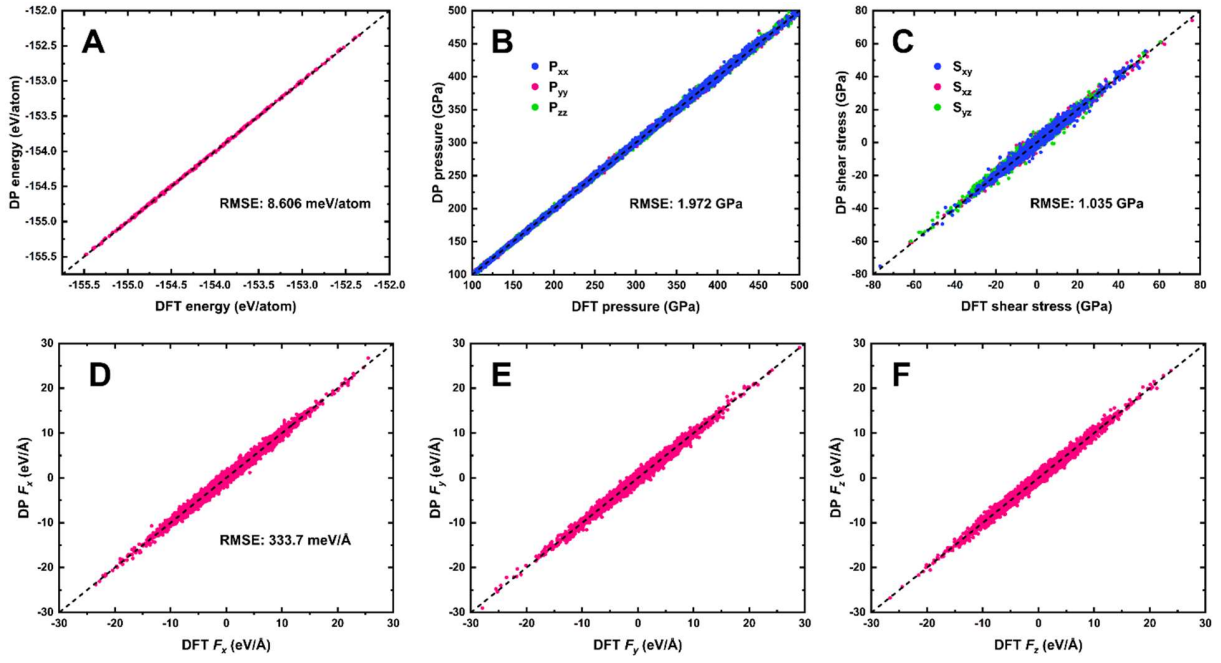


Fig. S3. Comparison of energies, stresses and forces calculated by DP and DFT. (A) Energies, (B) Normal Stresses, (C) Shear Stresses, and (D-F) Forces of both bcc and fcc configurations calculated at 100–500 GPa and 1000–5000 K. The dashed black line represents $y=x$, indicating that the predicted results by DP fit greatly with DFT.

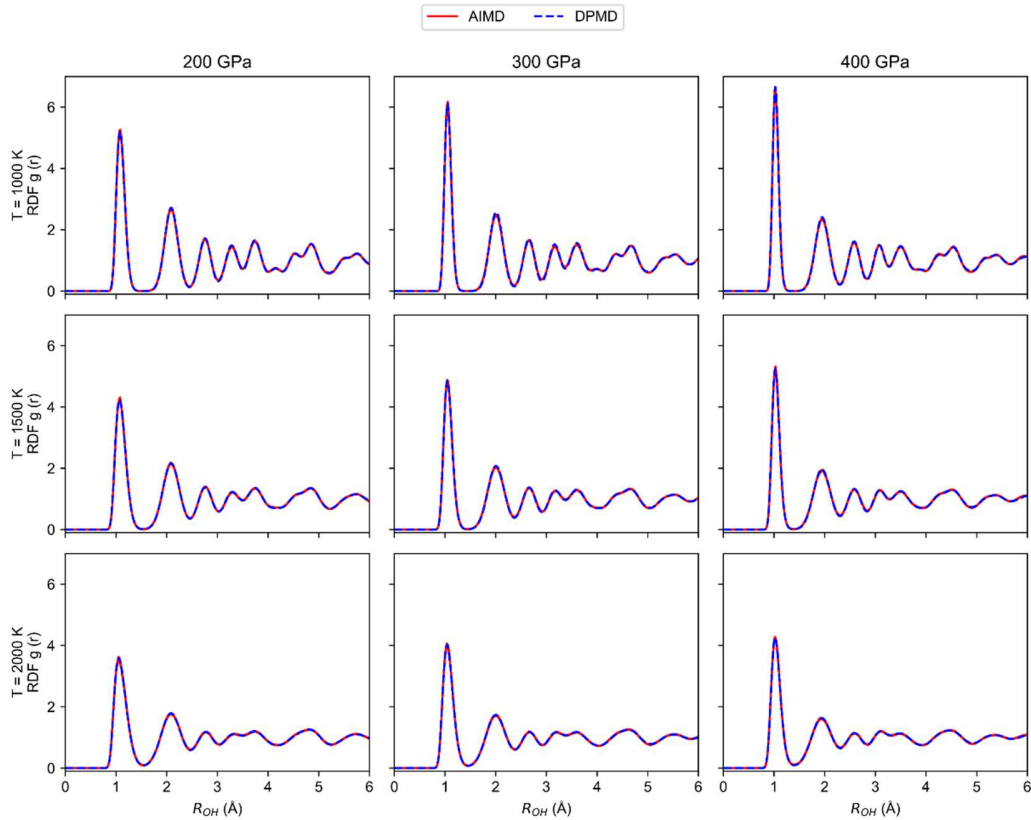


Fig. S4. Oxygen-hydrogen radial distribution functions of bcc H₂O calculated by DPMD and AIMD at 200–400 GPa and 1000–2000 K. The blue dashed lines represent the results from DPMD, and the red solid lines represent the results from AIMD. All the calculations were performed by employed *NVT* ensemble with 54 water molecules.

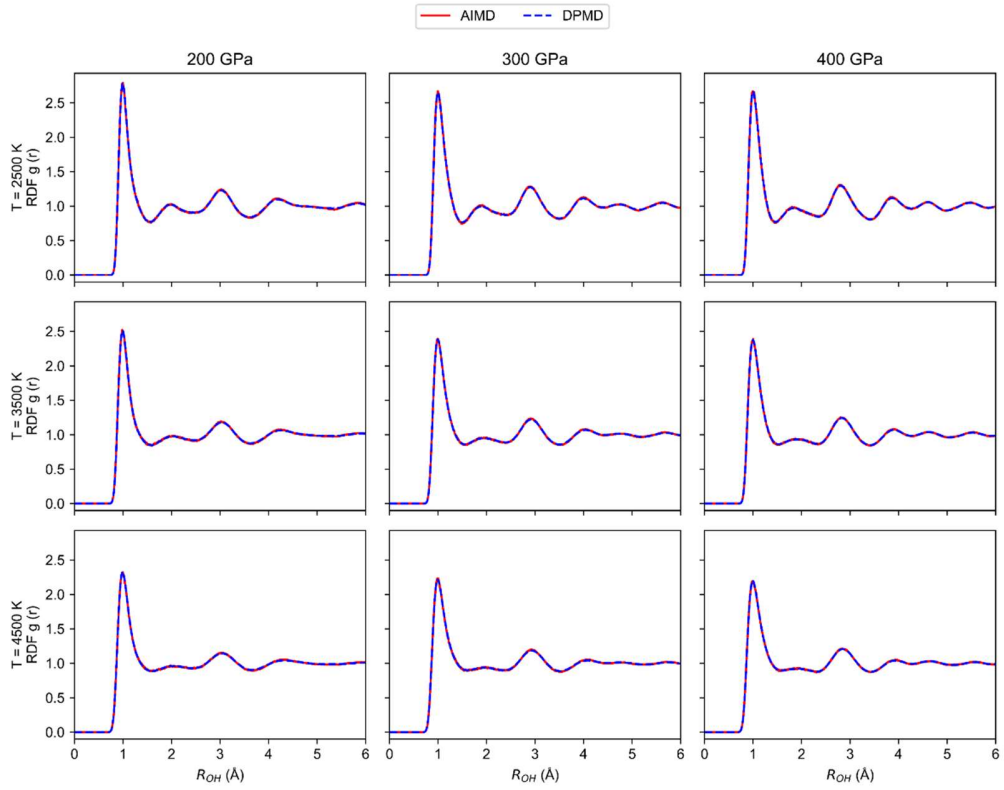


Fig. S5. Oxygen-hydrogen radial distribution functions of fcc H₂O calculated by DPMD and AIMD at 200–400 GPa and 2500–4500 K. The blue dashed lines represent the results from DPMD, and the red solid lines represent the results from AIMD. All the calculations were performed by employed *NVT* ensemble with 108 water molecules.

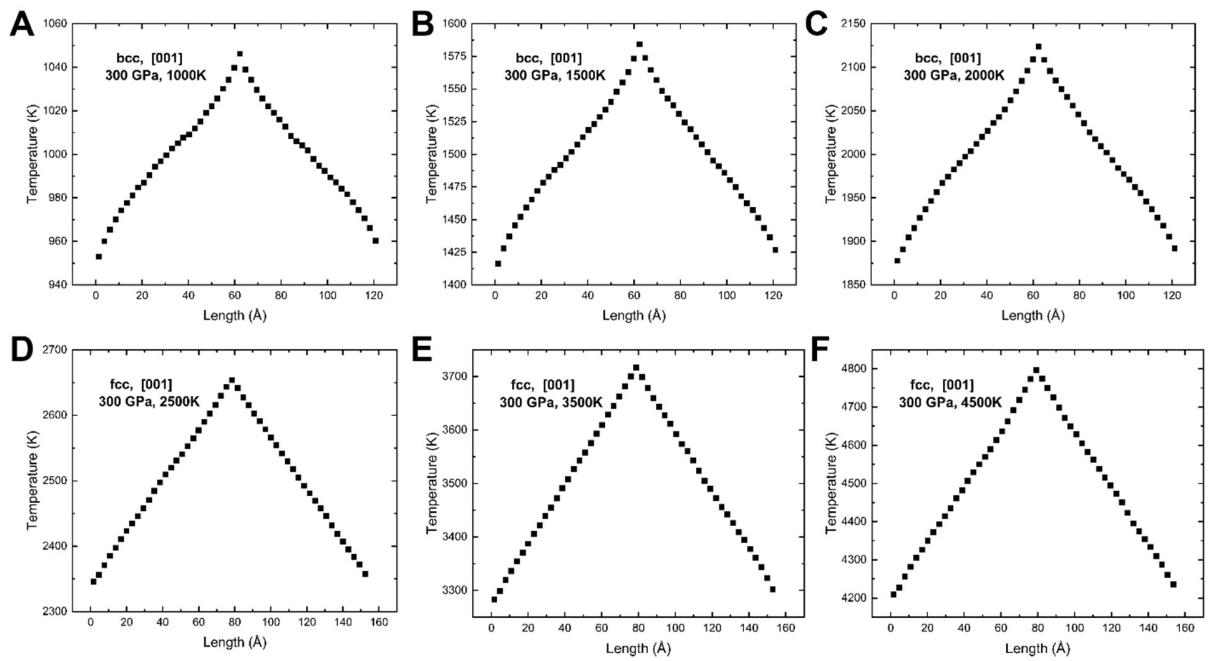


Fig. S6. Temperature gradient distribution along the heat transfer direction of (A–C) bcc ice and (D–F) fcc H₂O at 300 GPa from NEMD simulations. The percentage of non-linear regions is different in bcc and fcc phases. In the bcc H₂O, the non-linear region of the temperature gradient always exists at (A) 1000 K, (B) 1500 K, and (C) 2000 K, and this nonlinearity gradually weakens as the temperature increases. In the fcc H₂O, the non-linear region of the temperature gradient is almost nonexistent at (D) 2500 K, (E) 3500 K, and (F) 4500 K.

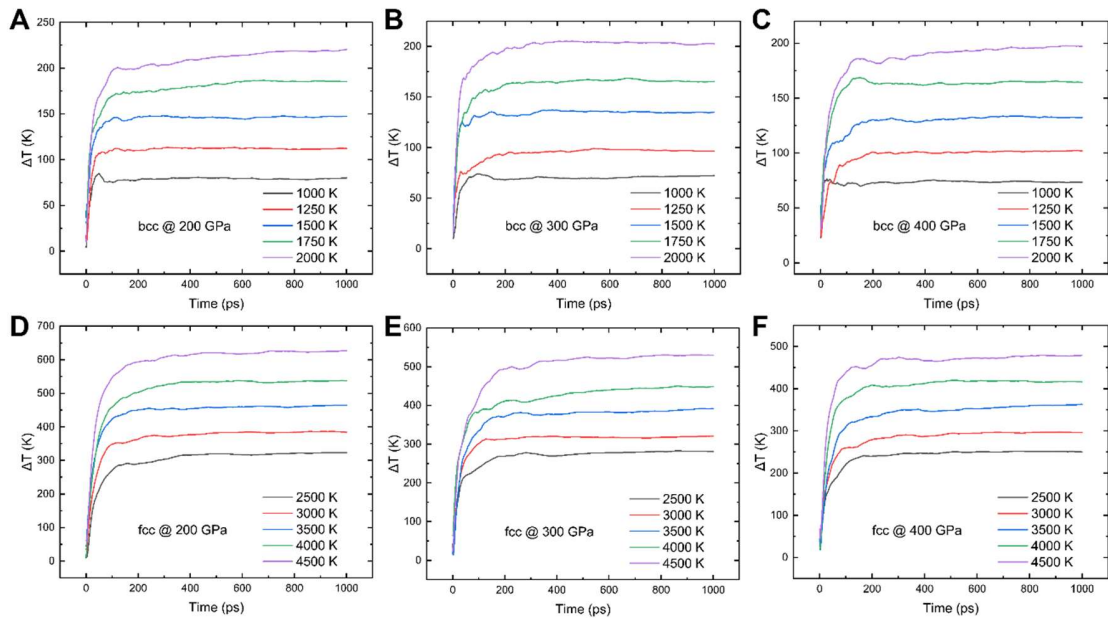


Fig. S7. Time convergence of temperature difference under imposed heat flux for (A–C) bcc and (D–F) fcc systems at different conditions. Curves of different colors correspond to simulations performed at temperatures ranging from 1000 K to 2000 K in bcc H₂O, at (A) 200 GPa, (B) 300 GPa, and (C) 400 GPa. Similarly, in an fcc H₂O with temperatures ranging from 2500 K to 4500 K, at (D) 200 GPa, (E) 300 GPa, and (F) 400 GPa.

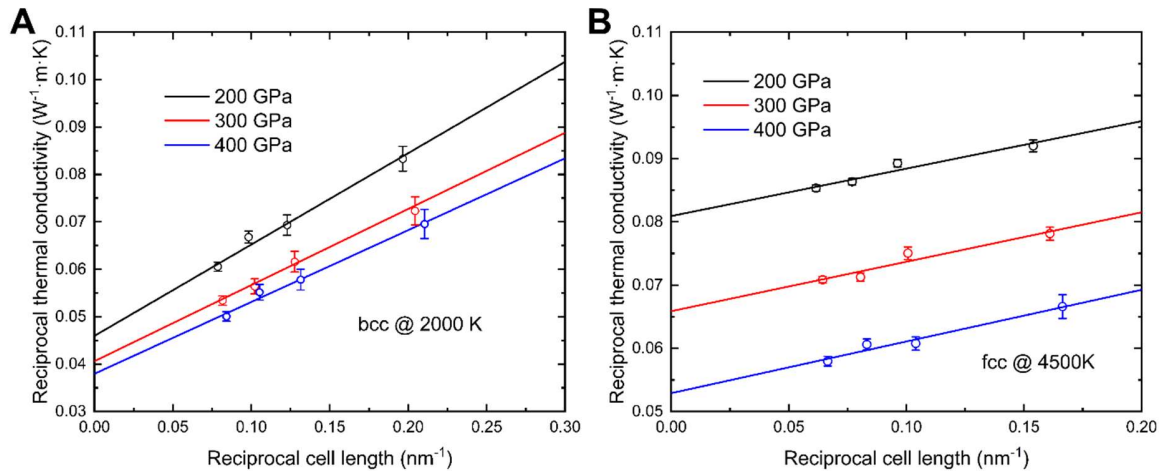


Fig. S8. Finite-size extrapolation of the reciprocal thermal conductivity for bcc and fcc H₂O at high pressures. (A) Reciprocal thermal conductivity of bcc phase at 2000 K as a function of the reciprocal cell length under 200, 300, and 400 GPa. (B) Reciprocal thermal conductivity of fcc phase at 4500 K as a function of the reciprocal cell length under 200, 300, and 400 GPa. Different colors represent different pressures, as indicated in the legends, and the error bars denote the standard deviations obtained from independent simulations.

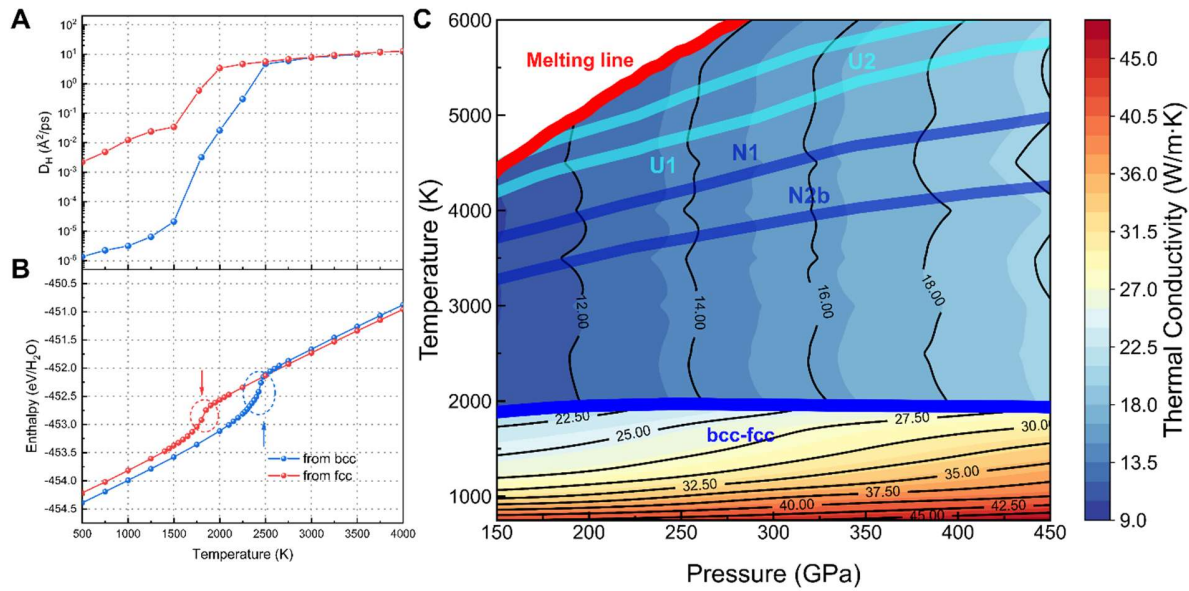


Fig. S9. Thermodynamic and thermal conductivity properties of bcc and fcc H₂O under high P-T. (A, B) The diffusion coefficients of hydrogen D_H and enthalpy per H₂O molecule for bcc phase (blue dotted line) and fcc phase (red dotted line) as a function of temperature along isobar of 200 GPa. The estimated superionic transition temperatures of bcc and fcc are indicated by the blue and red arrows. (C) The calculated thermal conductivity of bcc H₂O and fcc H₂O across a wide range of pressure and temperature conditions in the interior of Uranus and Neptune. The contour lines indicate the thermal conductivity. The blue and red lines separate different stability fields and phases, that is the bcc-fcc and fcc-liquid phase boundary (37). The cyan solid line represents the U1 and U2 models, corresponding to the thermal profile of Uranus's interior (40). The dark blue solid line represents the N1 and N2b models, corresponding to the thermal profile of Neptune's interior (40).

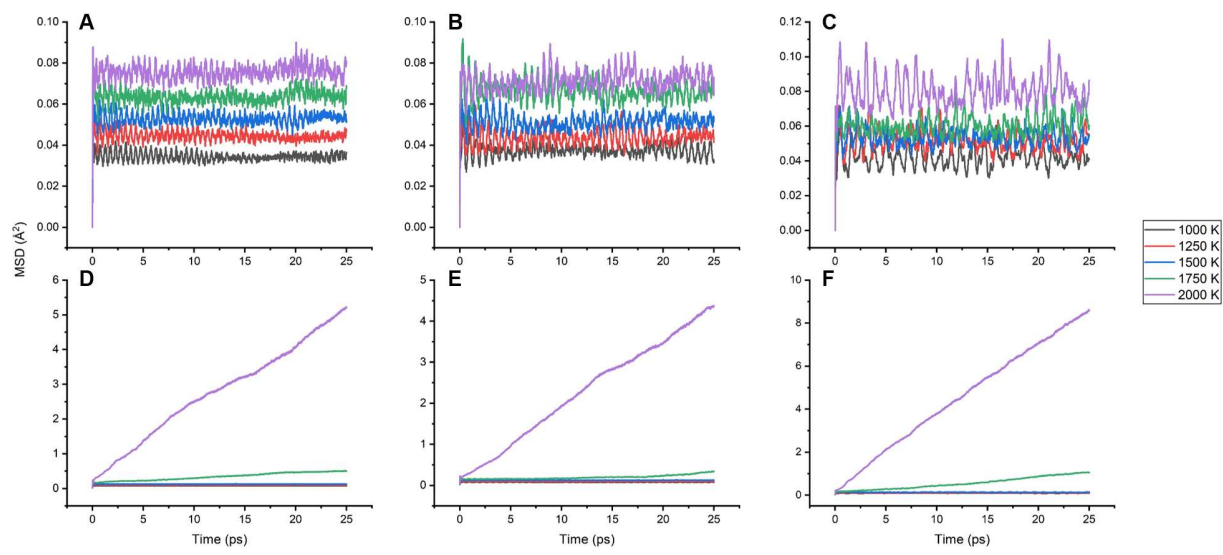


Fig. S10. Mean square displacements of (A–C) oxygen and (D–F) hydrogen in bcc H₂O at 200–400 GPa and 1000–2000 K. At pressures of (A, D) 200 GPa, (B, E) 300 GPa, and (C, F) 400 GPa, oxygen remains in a solid state, while hydrogen begins to undergo a liquid-like diffusion at 1750 K.

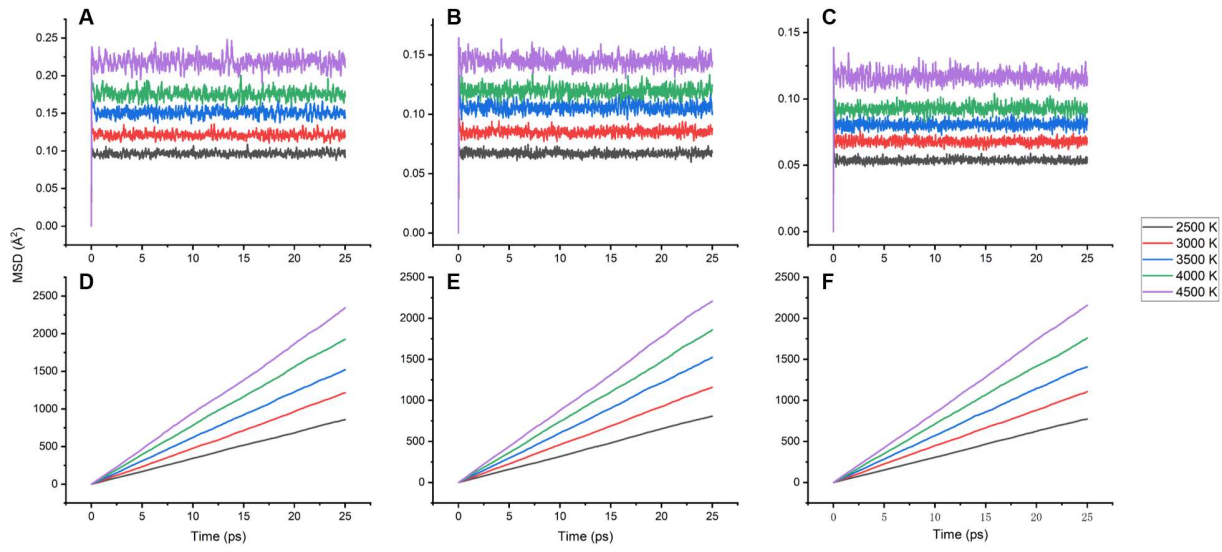


Fig. S11. Mean square displacements of (A–C) oxygen and (D–F) hydrogen in fcc H_2O at 200–400 GPa and 1000–2000 K. At pressures of (A, D) 200 GPa, (B, E) 300 GPa, and (C, F) 400 GPa, oxygen remains in a solid state, while hydrogen exhibits high diffusivity in the temperature range of 2500–4500 K.

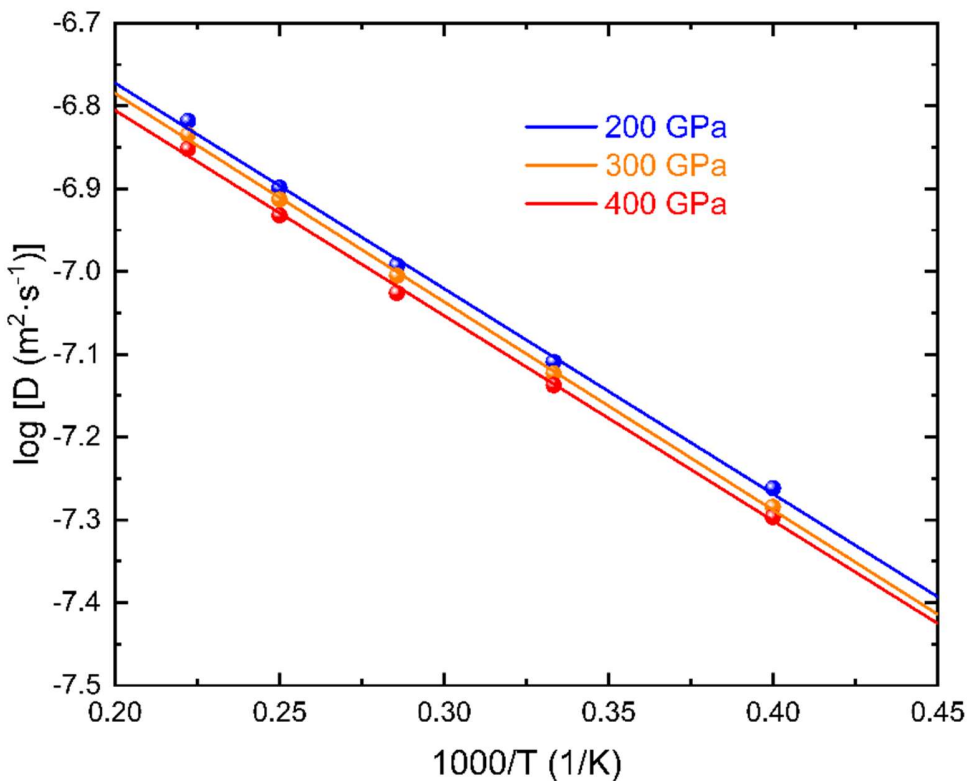


Fig. S12. The dependence of hydrogen diffusion coefficients on reciprocal of temperature in fcc H₂O at 200–400 GPa. Different diffusion coefficients at 200 GPa are shown in blue, 300 GPa in orange, and 400 GPa in red spheres, respectively. The diffusion coefficients are linearly fitted and shown with corresponding coloured lines.

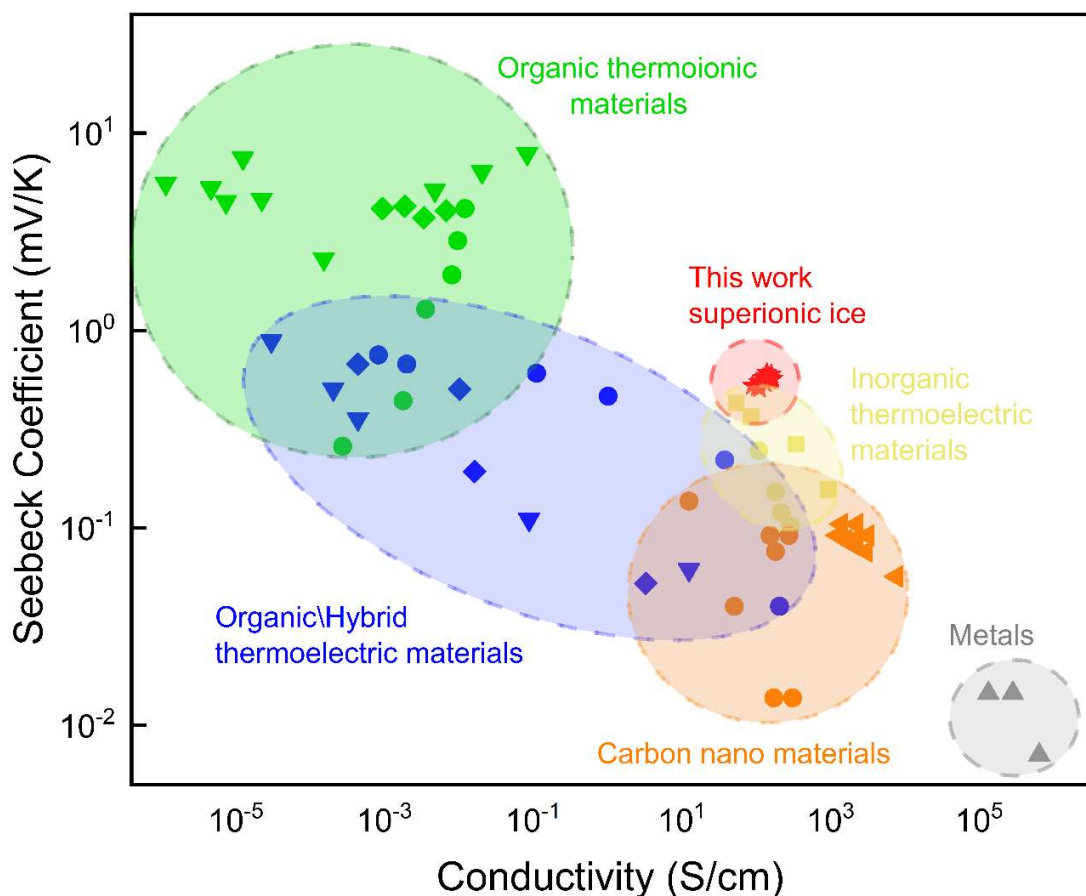


Fig. S13. Comparison of the Seebeck coefficients and conductivities of superionic H_2O ice with representative classes of thermoelectric, thermoionic and metal materials. The red symbols mark the values obtained in this work for superionic ice. The green, blue, orange, yellow, and grey shaded regions correspond to organic thermoionic materials, organic/hybrid thermoelectric materials, carbon nanomaterials, inorganic thermoelectric materials, and metals, respectively (88).

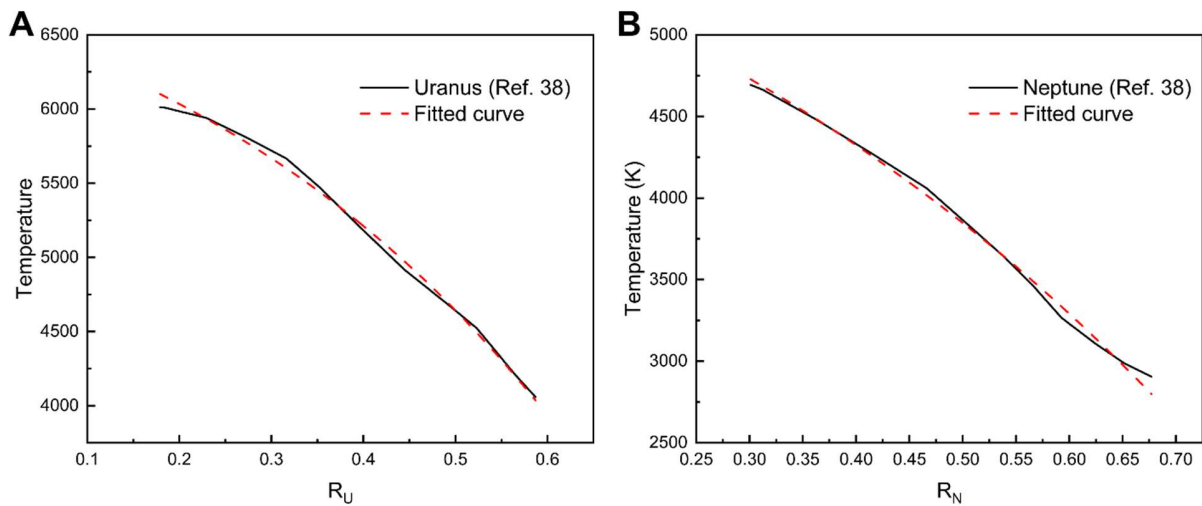


Fig. S14. Comparison between interior temperature profiles and fitted thermal curves for Uranus and Neptune. (A) Temperature profile of Uranus as a function of the normalized planetary radius R_U , showing the reference data from Ref. 40 (black solid) and the corresponding fitted curve (red dashed). (B) Temperature profile of Neptune as a function of the normalized planetary radius R_N , with the data from Ref. 40 (black solid) and the fitted curve (red dashed).

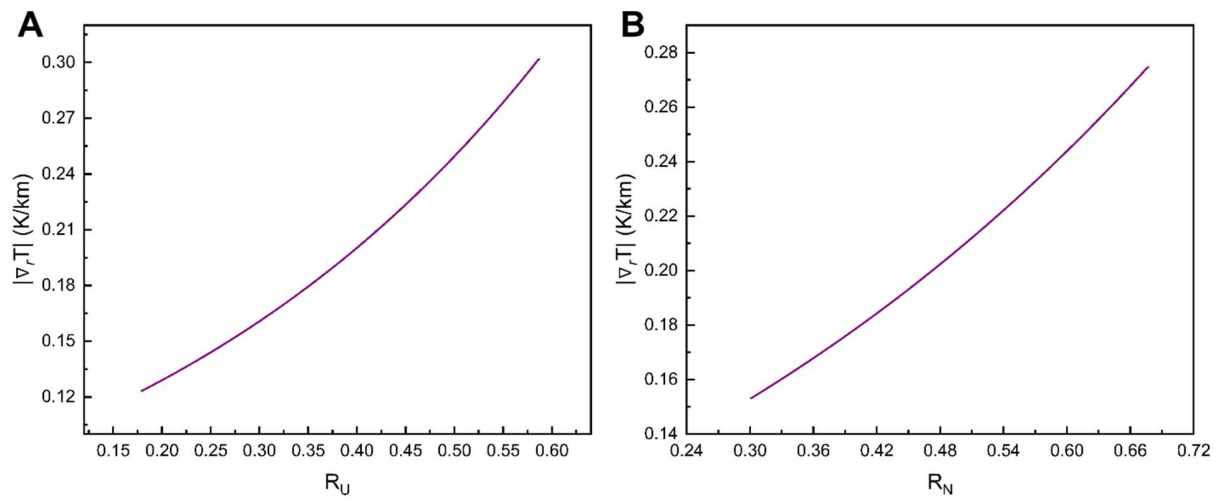


Fig. S15. Radial variation of the temperature gradient inside Uranus and Neptune derived from the fitted thermal profiles. (A) Magnitude of the temperature gradient $|\nabla_r T|$ in Uranus as a function of the normalized radius R_U . **(B)** Magnitude of the temperature gradient $|\nabla_r T|$ in Neptune as a function of the normalized radius R_N .

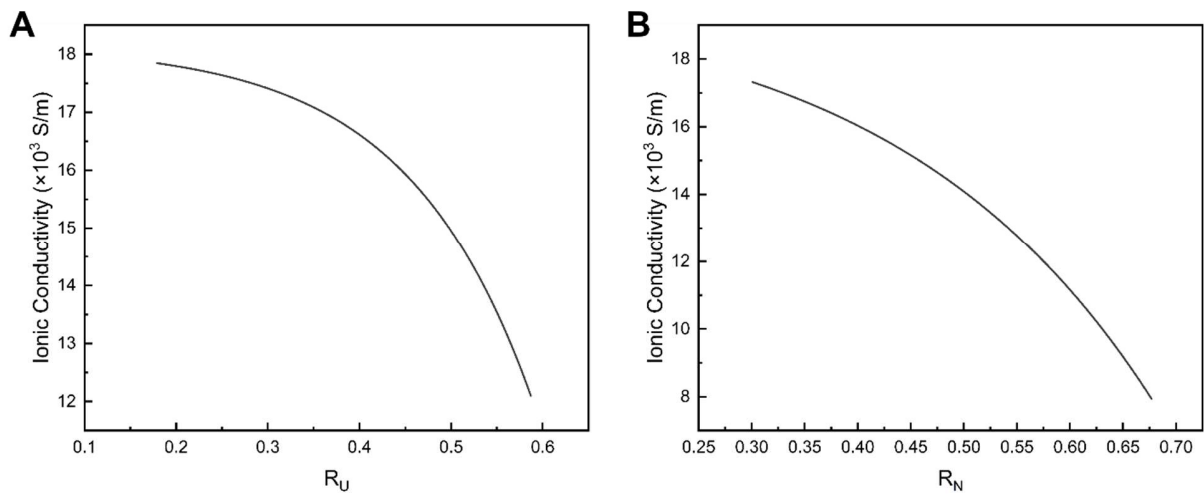


Fig. S16. Radial variation of ionic conductivities based on the internal thermal conditions of Uranus and Neptune. (A) Ionic conductivities of Uranus as a function of the normalized radius R_U . (B) Ionic conductivities of Neptune as a function of the normalized radius R_N . In both planets, the ionic conductivity decreases toward the outer layers, reflecting the combined effects of reduction of temperature and superionic conductivities.

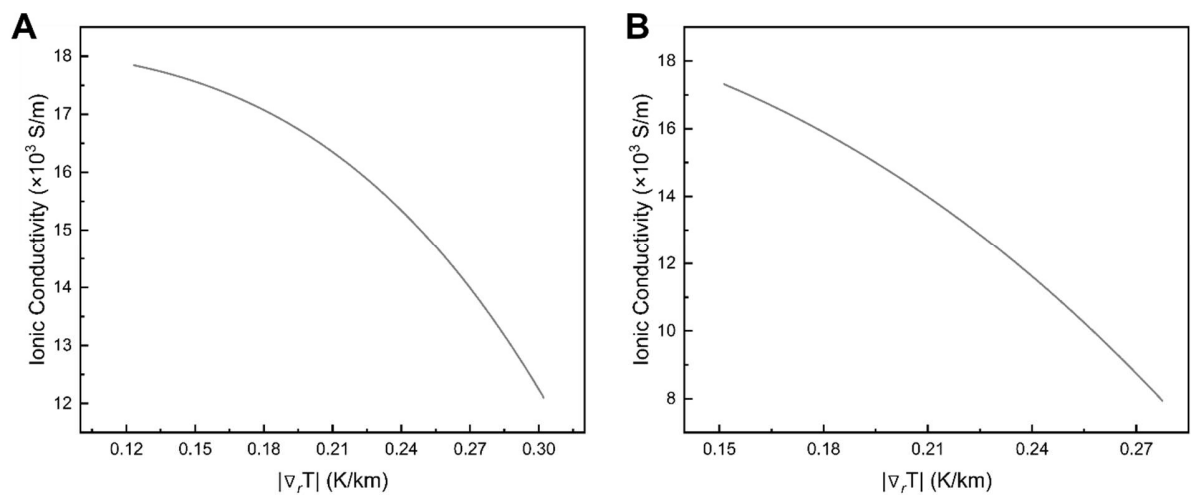


Fig. S17. Relationship between ionic conductivities and the temperature gradients in the interiors of Uranus and Neptune. Ionic conductivities of (A) Uranus and (B) Neptune as a function of the magnitude of the temperature gradient $|\nabla_r T|$.

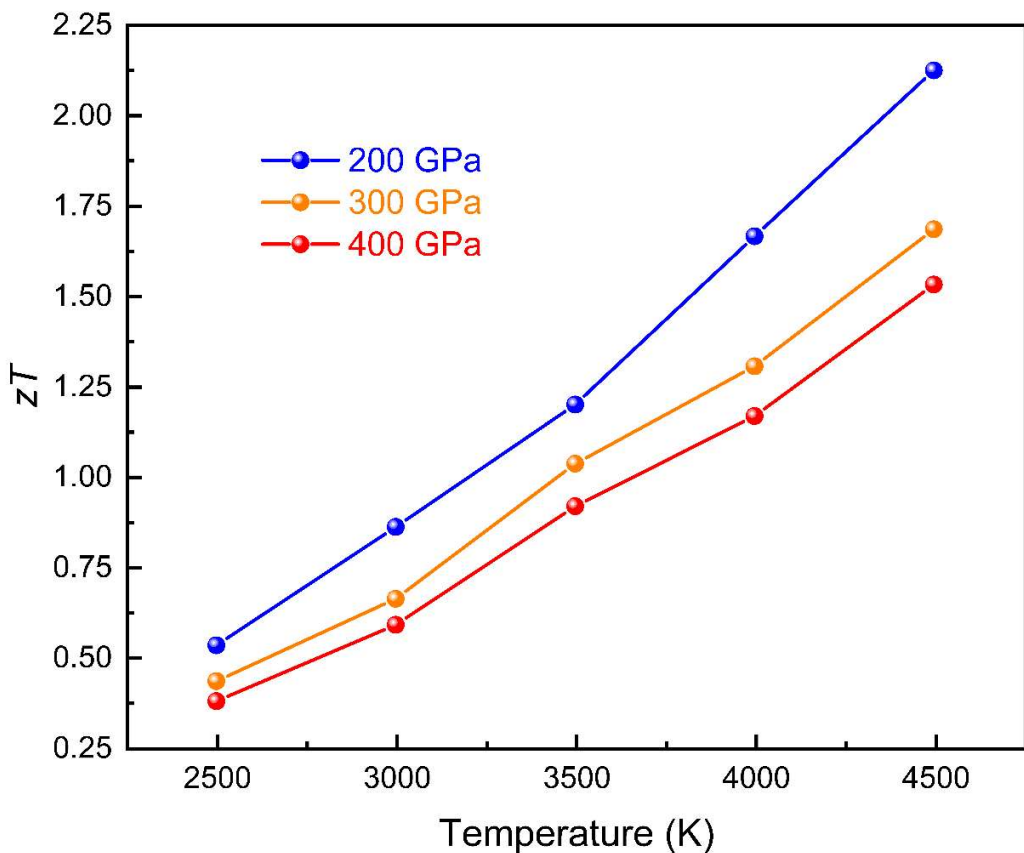


Fig. S18. Temperature dependence of the thermoelectric figure of merit zT for superionic H_2O ice at 200–400 GPa. The blue, orange, and red curves correspond to 200, 300, and 400 GPa, respectively.

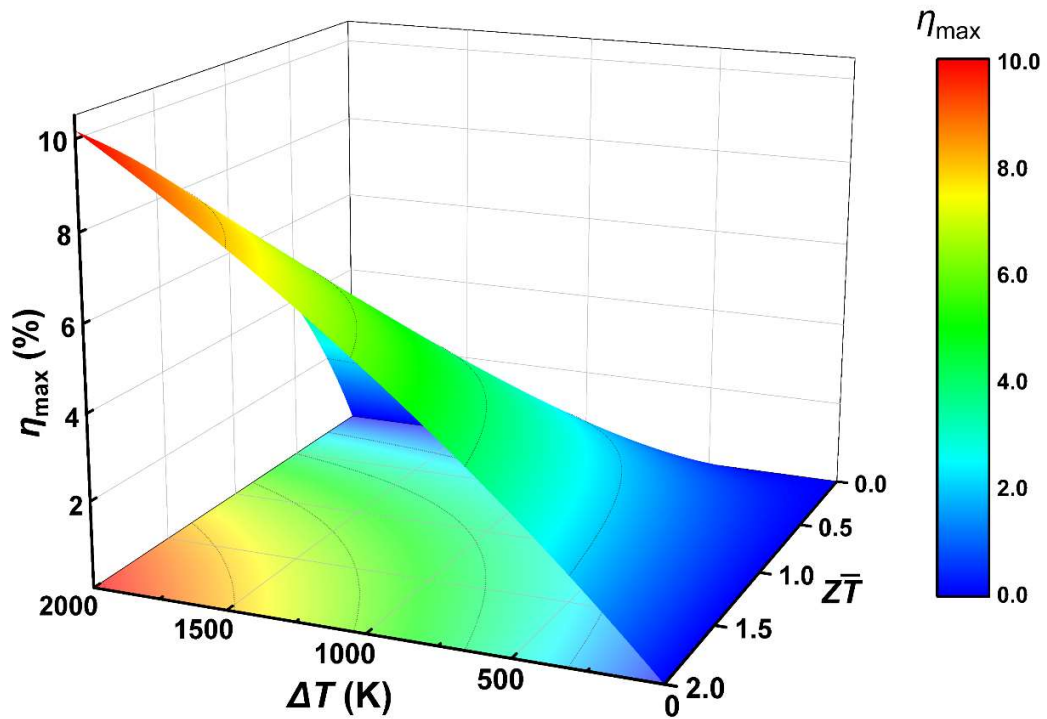


Fig. S19. Maximum thermoelectric conversion efficiency η_{\max} as a function of the temperature difference ΔT and the figure of merit \bar{ZT} . The three-dimensional surface illustrates the coupled dependence of η_{\max} on ΔT and \bar{ZT} , with colors indicating the corresponding efficiency values. Higher \bar{ZT} and larger ΔT jointly enhance thermoelectric conversion efficiency.

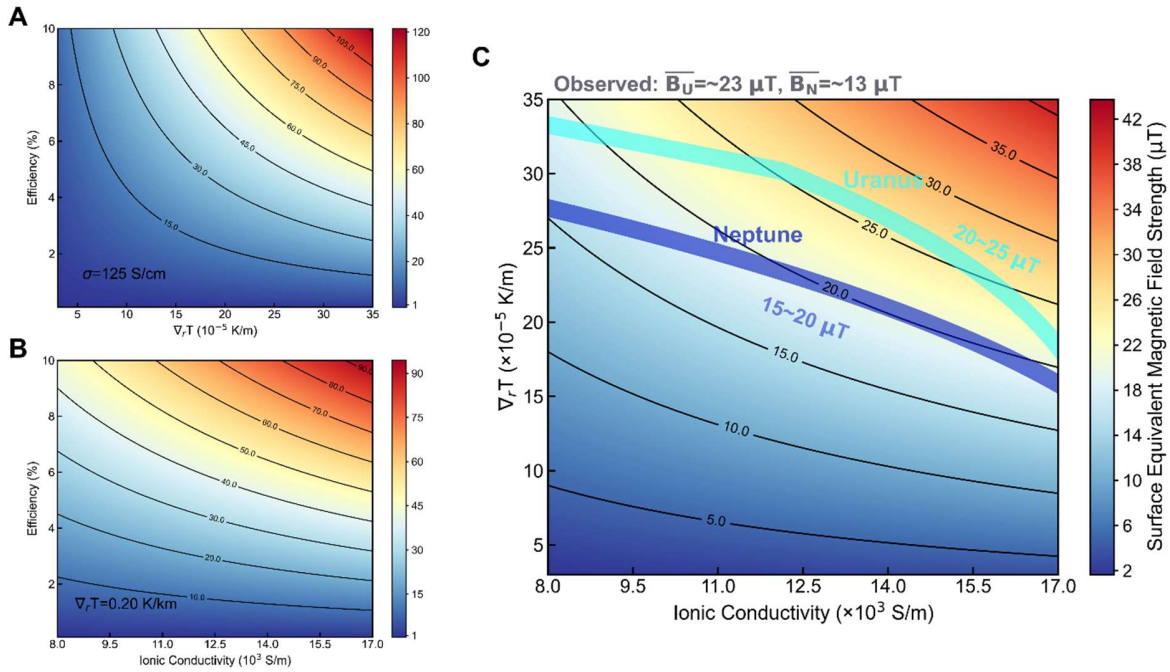


Fig. S20. The dependence of surface-equivalent magnetic strength on ionic conductivity, temperature gradient, and thermoelectric conversion efficiency. (A) Surface-equivalent magnetic flux density as a function of efficiency and radial temperature gradient, calculated at a fixed ionic conductivity of $\sigma = 125$ S/cm. (B) Surface-equivalent magnetic flux density as a function of efficiency and ionic conductivity, calculated at a fixed radial temperature gradient of $|\nabla_r T| = 0.20$ K/km. (C) Surface-equivalent magnetic strength as a function of ionic conductivity and radial temperature gradient for a fixed thermoelectric conversion efficiency of $\eta = 2.5\%$. The cyan and dark blue shaded bands highlight the predicted surface magnetic field strength based on the ionic conductivity and temperature gradient parameters of Uranus and Neptune. These regions present good consistency with the observed surface-equivalent magnetic field strength of Uranus ($\bar{B}_U \approx 23 \mu\text{T}$) (2) and Neptune ($\bar{B}_N \approx 13 \mu\text{T}$) (3).

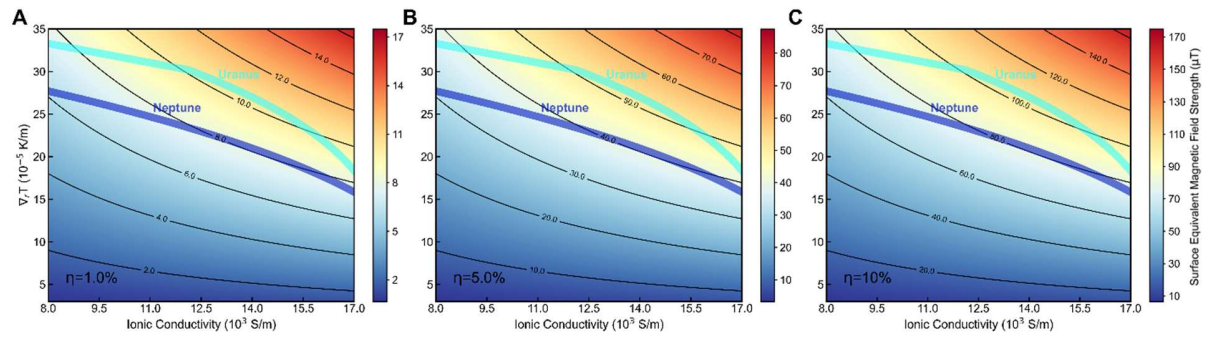


Fig. S21. Surface-equivalent magnetic strength generated by the thermoelectric mechanism under different conversion efficiencies. Comparing the magnetic strength at conversion efficiencies of (A) 1.0 %, (B) 5.0 %, and (C) 10.0 %. It indicates that the simulated magnetic strength based on thermoelectric generation mechanism is significantly affected by the conversion efficiency.

Table S1. The relevant data of the density (ρ), diffusion coefficient of hydrogen (D_H), and thermal conductivity (κ) of bcc H₂O ice in the pressure range of 200 GPa to 400 GPa, as the temperature increases from 1000 K to 2000 K.

Phase	Pressure (GPa)	Temperature (K)	ρ (g/cm ³)	D_H (m ² /s)	κ (W/m/K)
Ice X bcc	200	1000	3.69	2.45e-15	33.01
		1250	3.67	4.78e-14	27.68
		1500	3.66	3.62e-13	25.41
		1750	3.65	3.82e-11	23.39
		2000	3.64	3.25e-10	21.99
	300	1000	4.12	1.18e-15	36.98
		1250	4.11	1.67e-14	31.15
		1500	4.10	1.47e-13	28.27
		1750	4.09	3.31e-11	26.52
		2000	4.09	3.43e-10	24.88
	400	1000	4.49	2.23e-15	39.05
		1250	4.48	3.36e-14	34.76
		1500	4.47	1.01e-12	31.69
		1750	4.47	8.74e-11	28.82
		2000	4.46	8.72e-10	26.48

Table S2. The relevant data of the density (ρ), diffusion coefficient of hydrogen (D_H), thermal conductivity (κ), and ionic Seebeck coefficient (S_{td}) of fcc H₂O ice in the pressure range of 200 GPa to 400 GPa, as the temperature increases from 2500 K to 4500 K.

Phase	Pressure (GPa)	Temperature (K)	ρ (g/cm ³)	D_H (m ² /s)	κ (W/m/K)	S_{td} (μ V/K)
Ice XVIII fcc	200	2500	3.61	5.47e-8	12.32	528.39
		3000	3.58	7.78e-8	12.34	553.57
		3500	3.56	1.02e-7	12.53	574.88
		4000	3.53	1.26e-7	12.26	592.93
		4500	3.50	1.52e-7	12.38	609.41
	300	2500	4.11	5.19e-8	15.13	516.47
		3000	4.08	7.53e-8	15.33	541.29
		3500	4.05	9.89e-8	15.18	561.89
		4000	4.03	1.22e-7	15.44	580.84
		4500	4.00	1.46e-7	15.25	596.38
	400	2500	4.51	5.05e-8	18.56	507.98
		3000	4.48	7.29e-8	18.27	532.49
		3500	4.46	9.42e-8	18.61	533.47
		4000	4.43	1.17e-7	18.19	571.36
		4500	4.41	1.41e-7	18.64	587.39

References

1. C. T. Russell, Magnetic fields of the terrestrial planets. *J. Geophys. Res. Planets* 98, 18681–18695 (1993).
2. N. F. Ness, M. H. Acuña, K. W. Behannon, L. F. Burlaga, J. E. P. Connerney, R. P. Lepping, F. M. Neubauer, Magnetic Fields at Uranus. *Science* 233, 85–89 (1986).
3. N. F. Ness, M. H. Acuña, L. F. Burlaga, J. E. P. Connerney, R. P. Lepping, F. M. Neubauer, Magnetic Fields at Neptune. *Science* 246, 1473–1478 (1989).
4. G. Schubert, K. M. Soderlund, Planetary magnetic fields: Observations and models. *Phys. Earth Planet. Inter.* 187, 92–108 (2011).
5. R. Redmer, T. R. Mattsson, N. Nettelmann, M. French, The phase diagram of water and the magnetic fields of Uranus and Neptune. *Icarus* 211, 798–803 (2011).
6. C. Paty, C. S. Arridge, I. J. Cohen, G. A. DiBraccio, R. W. Ebert, A. M. Rymer, Ice giant magnetospheres. *Phil. Trans. R. Soc. A* 378, 20190480 (2020).
7. K. M. Soderlund, S. Stanley, The underexplored frontier of ice giant dynamos. *Phil. Trans. R. Soc. A* 378, 20190479 (2020).
8. S. Stanley, J. Bloxham, Convective-region geometry as the cause of Uranus' and Neptune's unusual magnetic fields. *Nature* 428, 151–153 (2004).
9. B. Militzer, Phase separation of planetary ices explains nondipolar magnetic fields of Uranus and Neptune. *Proc. Natl. Acad. Sci.* 121, e2403981121 (2024).
10. K. Soderlund, M. Heimpel, E. King, J. Aurnou, Turbulent models of ice giant internal dynamics: Dynamos, heat transfer, and zonal flows. *Icarus* 224, 97–113 (2013).
11. M. Podolak, A. Weizman, M. Marley, Comparative models of Uranus and Neptune. *Planet. Space Sci.* 43, 1517–1522 (1995).
12. J.-A. Hernandez, M. Bethkenhagen, S. Ninet, M. French, A. Benuzzi-Mounaix, F. Datchi, M. Guaraguaglini, F. Lefevre, F. Occelli, R. Redmer, T. Vinci, A. Ravasio, Melting curve of superionic ammonia at planetary interior conditions. *Nat. Phys.* 19, 1280–1285 (2023).
13. A. F. Goncharov, N. Goldman, L. E. Fried, J. C. Crowhurst, I. -F. W. Kuo, C. J. Mundy, and J. M. Zaug, Dynamic ionization of water under extreme conditions. *Phys. Rev. Lett.* 94, 125508 (2005).
14. K. de Villa, F. González-Cataldo, B. Militzer, Double superionicity in icy compounds at planetary interior conditions. *Nat. Commun.* 14, 7580 (2023).

15. C. Cavazzoni, G. L. Chiarotti, S. Scandolo, E. Tosatti, M. Bernasconi, M. Parrinello, Superionic and metallic states of water and ammonia at giant planet conditions. *Science* 283, 44–46 (1999).
16. E. Katoh, H. Yamawaki, H. Fujihisa, M. Sakashita, K. Aoki, Protonic diffusion in high-pressure ice VII. *Science* 295, 1264–1266 (2002).
17. M. French, S. Hamel, R. Redmer, Dynamical screening and ionic conductivity in water from ab initio simulations. *Phys. Rev. Lett.* 107, 185901 (2011).
18. J. -A. Hernandez, R. Caracas, Superionic-superionic phase transitions in body-centered cubic H₂O ice. *Phys. Rev. Lett.* 117, 135503 (2016).
19. M. Millot, S. Hamel, J. R. Rygg, P. M. Celliers, G. W. Collins, F. Coppapi, D. E. Fratanduono, R. Jeanloz, D. C. Swift, J. H. Eggert, Experimental evidence for superionic water ice using shock compression. *Nat. Phys.* 14, 297–302 (2018).
20. J.-A. Queyroux, J. -A. Hernandez, G. Weck, S. Ninet, T. Plisson, S. Klotz, G. Garbarino, N. Guignot, M. Mezouar, M. Hanfland, J.-P. Itié, F. Datchi, Melting curve and isostructural solid transition in superionic ice. *Phys. Rev. Lett.* 125, 195501 (2020).
21. B. Cheng, M. Bethkenhagen, C. J. Pickard, S. Hamel, Phase behaviours of superionic water at planetary conditions. *Nat. Phys.* 17, 1228–1232 (2021).
22. M. Millot, F. Coppapi, J. R. Rygg, A. Correa Barrios, S. Hamel, D. C. Swift, J. H. Eggert, Nanosecond X-ray diffraction of shock-compressed superionic water ice. *Nature* 569, 251–255 (2019).
23. V. B. Prakapenka, N. Holtgrewe, S. S. Lobanov, A. F. Goncharov, Structure and properties of two superionic ice phases. *Nat. Phys.* 17, 1233–1238 (2021).
24. G. Weck, J. -A. Queyroux, S. Ninet, F. Datchi, M. Mezouar, P. Loubeyre, Evidence and stability field of fcc superionic water ice using static compression. *Phys. Rev. Lett.* 128, 165701 (2022).
25. S. Sun, Y. He, D. Y. Kim, H. Li, Anomalous elastic properties of superionic ice. *Phys. Rev. B* 102, 104108 (2020).
26. F. Matusalem, J. Santos Rego, M. de Koning, Plastic deformation of superionic water ices. *Proc. Natl. Acad. Sci.* 119, e2203397119 (2022).
27. R. J. Husband, H. P. Liermann, J. D. McHardy, R. S. McWilliams, A. F. Goncharov, V. B. Prakapenka, E. Edmund, S. Chariton, Z. Konôpková, C. Strohm, C. Sanchez-Valle, M.

Frost, L. Andriambariarijaona, K. Appel, C. Baehtz, O. B. Ball, R. Briggs, J. Buchen, V. Cerantola, J. Choi, A. L. Coleman, H. Cynn, A. Dwivedi, H. Graafsma, H. Hwang, E. Koemets, T. Laurus, Y. Lee, X. Li, H. Marquardt, A. Mondal, M. Nakatsutsumi, S. Ninet, E. Pace, C. Pepin, C. Prescher, S. Stern, J. Sztuk-Dambietz, U. Zastrau, M. I. McMahon, Phase transition kinetics of superionic H₂O ice phases revealed by Megahertz X-ray free-electron laser-heating experiments. *Nat. Commun.* 15, 8256 (2024).

28. E. Sugimura, T. Komabayashi, K. Ohta, K. Hirose, Y. Ohishi, L. S. Dubrovinsky, Experimental evidence of superionic conduction in H₂O ice. *J. Chem. Phys.* 137, 194505 (2012).

29. F. Grasselli, L. Stixrude, S. Baroni, Heat and charge transport in H₂O at ice-giant conditions from ab initio molecular dynamics simulations. *Nat. Commun.* 11, 3605 (2020).

30. L. Stixrude, S. Baroni, F. Grasselli, Thermal and tidal evolution of Uranus with a growing frozen core. *Planet. Sci. J.* 2, 222 (2021).

31. H. Wang, U. Ail, R. Gabrielsson, M. Berggren, X. Crispin, Ionic Seebeck Effect in Conducting Polymers. *Adv. Energy Mater.* 5, 1500044 (2015).

32. C. G. Han, X. Qian, Q. Li, B. Deng, Y. Zhu, Z. Han, W. Zhang, W. Wang, S. P. Feng, G. Chen, W. Liu, Giant thermopower of ionic gelatin near room temperature. *Science* 368, 1091–1098 (2020).

33. C. Chi, M. An, X. Qi, Y. Li, R. Zhang, G. Liu, C. Lin, H. Huang, H. Dang, B. Demir, Y. Wang, W. Ma, B. Huang, X. Zhang, Selectively tuning ionic thermopower in all-solid-state flexible polymer composites for thermal sensing. *Nat. Commun.* 13, 221 (2022).

34. N. Jabeen, M. Muddasar, N. Menéndez, M. A. Nasiri, C. M. Gómez, M. N. Collins, R. Muñoz-Espí, A. Cantarero, M. Culebras, Recent advances in ionic thermoelectric systems and theoretical modelling. *Chem. Sci.* 15, 14122–14153 (2024).

35. O. Nickel, L. J. V. Ahrens-Iwers, R. H. Meißner, M. Janssen, Water, not salt, causes most of the Seebeck effect of nonisothermal aqueous electrolytes. *Phys. Rev. Lett.* 132, 186201 (2024).

36. X. Qian, Z. Ma, Q. Huang, H. Jiang, R. Yang, Thermodynamics of ionic thermoelectrics for low-grade heat harvesting. *ACS Energy Lett.* 9, 679–706 (2024).

37. A. Forestier, G. Weck, F. Datchi, S. Ninet, G. Garbarino, M. Mezouar, P. Loubeyre, X-ray signature of the superionic transition in warm dense fcc water ice. *Phys. Rev. Lett.* 134, 076102 (2025).
38. N. I. Pavlenko, I. V. Stasyuk, The effect of proton interactions on the conductivity behavior in systems with superionic phases. *J. Chem. Phys.* 114, 4607–4617 (2001).
39. M. French, M. P. Desjarlais, R. Redmer, Ab initio calculation of thermodynamic potentials and entropies for superionic water. *Phys. Rev. E.* 93, 022140 (2016).
40. N. Nettelmann, R. Helled, J. J. Fortney, R. Redmer, New indication for a dichotomy in the interior structure of Uranus and Neptune from the application of modified shape and rotation data. *Planet. Space Sci.* 77, 143–151 (2013).
41. A. Sohn, C. Yu, Ionic transport properties and their empirical correlations for thermal-to-electrical energy conversion. *Mater. Today Phys.* 19, 100433 (2021).
42. S. Sun, M. Li, X. L. Shi, Z. G. Chen, Advances in ionic thermoelectrics: from materials to devices. *Adv. Energy Mater.* 13, 2203692 (2023).
43. A. C. Mitchell, W. J. Nellis, Equation of state and electrical conductivity of water and ammonia shocked to the 100 GPa (1 Mbar) pressure range. *J. Chem. Phys.* 76, 6273-6281 (1982).
44. K. Oka, Y. Okuda, K. Hirose, Hot interiors of ice giant planets inferred from electrical conductivity of dense H₂O fluid. *arXiv preprint arXiv*, 2401.11454, (2024).
45. B. Militzer, Ab Initio Entropy Calculations of Water Predict the Interiors of Uranus and Neptune to Be 15%–30% Colder than Previous Models. *Astrophys. J.* 990, 20 (2025).
46. S. Markham, D. Stevenson, Constraining the effect of convective inhibition on the thermal evolution of Uranus and Neptune. *Planet. Sci. J.* 2, 146 (2021).
47. N. Nettelmann, K. Wang, J. J. Fortney, S. Hamel, S. Yellamilli, M. Bethkenhagen, R. Redmer, Uranus evolution models with simple thermal boundary layers. *Icarus* 275, 107–116 (2016).
48. M. Podolak, R. Helled, G. Schubert, Effect of non-adiabatic thermal profiles on the inferred compositions of Uranus and Neptune. *Mon. Not. R. Astron. Soc.* 487, 2653–2664 (2019).
49. L. Scheibe, N. Nettelmann, R. Redmer, Thermal evolution of Uranus and Neptune-II. Deep thermal boundary layer. *Astron. Astrophys.* 650, A200 (2021).

50. H. Ravit, N. Nadine, G. Tristan, Uranus and Neptune: Origin, Evolution and Internal Structure. *Space Sci. Rev.* 216, 38 (2020).

51. A. N. Dmitriev, Thermoelectric Currents of Earth's Core Generate the Earth's Magnetic Field. *Int. J. Geosci.* 8, 1048–1071 (2017).

52. S. Pan, T. Huang, A. Vazan, Z. Liang, C. Liu, J. Wang, C. J. Pickard, H. T. Wang, D. Xing, J. Sun, Magnesium oxide-water compounds at megabar pressure and implications on planetary interiors. *Nat. Commun.* 14, 1165 (2023).

53. H. Gao, C. Liu, J. Shi, S. Pan, T. Huang, X. Lu, H. -T. Wang, D. Xing, J. Sun, Superionic Silica-Water and Silica-Hydrogen Compounds in the Deep Interiors of Uranus and Neptune. *Phys. Rev. Lett.* 128, 035702 (2022).

54. W. Kohn, L. J. Sham, Self-consistent equations including exchange and correlation effects. *Phys. Rev.* 140, A1133 (1965).

55. R. Iftimie, P. Minary, M. E. Tuckerman, Ab initio molecular dynamics: Concepts, recent developments, and future trends. *Proc. Natl. Acad. Sci.* 102, 6654–6659 (2005).

56. M. Chen, G. C. Guo, L. He, Systematically improvable optimized atomic basis sets for ab initio calculations. *J. Phys-Condens. Matter.* 22, 445501 (2010).

57. P. Li, X. Liu, M. Chen, P. Lin, X. Ren, L. Lin, C. Yang, L. He, Large-scale ab initio simulations based on systematically improvable atomic basis. *Comput. Mater. Sci.* 112, 503–517 (2016).

58. P Lin, X Ren, X Liu, L He, Ab initio electronic structure calculations based on numerical atomic orbitals: Basic fomalisms and recent progresses. *Wiley Interdiscip. Rev. Comput. Mol. Sci.* 14, e1687 (2024).

59. J. P. Perdew, K. Burke, M. Ernzerhof, Generalized gradient approximation made simple. *Phys. Rev. Lett.* 77, 3865 (1996).

60. S. Grimme, J. Antony, S. Ehrlich, H. Krieg, A consistent and accurate ab initio parametrization of density functional dispersion correction (DFT-D) for the 94 elements H-Pu. *J. Chem. Phys.* 132, 154104 (2010).

61. D. R. Hamann, Optimized norm-conserving Vanderbilt pseudopotentials. *Phys. Rev. B.* 88, 085117 (2013).

62. K. G. Dyall, Relativistic double-zeta, triple-zeta, and quadruple-zeta basis sets for the 4s, 5s, 6s, and 7s elements. *J. Phys. Chem. A.* 113, 12638–12644 (2009).

63. L. Zhang, J. Han, H. Wang, W. Saidi, R. Car, End-to-end symmetry preserving inter-atomic potential energy model for finite and extended systems. *Adv. Neural Inform. Process. Syst.* 31, 4436–4446 (2018).

64. H. Wang, L. Zhang, J. Han, DeePMD-kit: A deep learning package for many-body potential energy representation and molecular dynamics. *Comput. Phys. Commun.* 228, 178–184 (2018).

65. L. Zhang, J. Han, H. Wang, R. Car, W. E, Deep potential molecular dynamics: a scalable model with the accuracy of quantum mechanics. *Phys. Rev. Lett.* 120, 143001 (2018).

66. J. Zeng et al., DeePMD-kit v2: A software package for deep potential models. *J. Chem. Phys.* 159, 054801 (2023).

67. T. Wen, L. Zhang, H. Wang, D. J. Srolovitz, Deep potentials for materials science. *Mater. Futures* 1, 022601 (2022).

68. Y. Zhang, H. Wang, W. Chen, J. Zeng, L. Zhang, H. Wang, DP-GEN: A concurrent learning platform for the generation of reliable deep learning based potential energy models. *Comput. Phys. Commun.* 253, 107206 (2020).

69. D. P. Kingma, J. Ba, Adam: A method for stochastic optimization. *arXiv preprint arXiv*, 1412.6980, (2014).

70. S. Plimpton, Fast parallel algorithms for short-range molecular dynamics. *J. Comput. Phys.* 117, 1–19 (1995).

71. T. Schneider, E. Stoll, Molecular-dynamics study of a three-dimensional one-component model for distortive phase transitions. *Phys. Rev. B.* 17, 1302 (1978).

72. A. P. Thompson et al., LAMMPS-a flexible simulation tool for particle-based materials modeling at the atomic, meso, and continuum scales. *Comput. Phys. Commun.* 271, 108171 (2022).

73. W. G. Hoover, Canonical dynamics: Equilibrium phase-space distributions. *Phys. Rev. A.* 31, 1695 (1985).

74. X. Michalet, Mean square displacement analysis of single-particle trajectories with localization error: Brownian motion in an isotropic medium. *Phys. Rev. E.* 82, 041914 (2010).

75. H. Qian, M. P. Sheetz, E. L. Elson, Single particle tracking. Analysis of diffusion and flow in two-dimensional systems. *Biophys. J.* 60, 910–921 (1991).

76. F. Müller-Plathe, A simple nonequilibrium molecular dynamics method for calculating the thermal conductivity. *J. Chem. Phys.* 106, 6082–6085 (1997).
77. C. Nieto-Draghi, J. B. Avalos, Non-equilibrium momentum exchange algorithm for molecular dynamics simulation of heat flow in multicomponent systems. *Mol. Phys.* 101, 2303–2307 (2003).
78. S. Stackhouse, L. Stixrude, B. B. Karki, Thermal conductivity of periclase (MgO) from first principles. *Phys. Rev. Lett.* 104, 208501 (2010).
79. P. K. Schelling, S. R. Phillpot, P. Kebinski, Comparison of atomic-level simulation methods for computing thermal conductivity. *Phys. Rev. B.* 65, 144306 (2002).
80. R. K. Pathria, P. D. Beale, *Statistical Mechanics* (Academic Press, 2011).
81. S. Duhr, D. Braun, Why molecules move along a temperature gradient. *Proc. Natl. Acad. Sci.* 103, 19678–19682 (2006).
82. C. G. Han, X. Qian, Q. Li, B. Deng, Y. Zhu, Z. Han, W. Zhang, W. Wang, S. P. Feng, G. Chen, W. Liu, Giant thermopower of ionic gelatin near room temperature. *Science* 368, 1091–1098 (2020).
83. L. Rezende Franco, A. L. Sehnem, A. M. Figueiredo Neto, K. Coutinho, Molecular dynamics approach to calculate the thermodiffusion (Soret and Seebeck) coefficients of salts in aqueous solutions. *J. Chem. Theory Comput.* 17, 3539–3553 (2021).
84. J. Kärger, D. M. Ruthven, D. N. Theodorou, *Diffusion in Nanoporous Materials* (Weinheim: Wiley-VCH, 2012).
85. B. Widom, Some topics in the theory of fluids. *J. Chem. Phys.* 39, 2808–2812 (1963).
86. J. Fourier, *The Analytical Theory of Heat* (Cambridge University Press, 1878).
87. D. Zhao, A. Würger, X. Crispin, Ionic thermoelectric materials and devices. *Journal of Energy Chemistry*. *J. Energy Chem.* 61, 88–103 (2021).
88. M. Massetti, F. Jiao, A. J. Ferguson, D. Zhao, K. Wijeratne, A. Würger, J. L. Blackburn, X. Crispin, S. Fabiano, Unconventional thermoelectric materials for energy harvesting and sensing applications. *Chem. Rev.* 121, 12465–12547 (2021).